MOUNTAIN-PLAINS CONSORTIUM

MPC 24-524 | C. Pantelides, S. Neupane, and D. Tran

NUMERICAL ANALYSIS OF ABC HYBRID BRIDGE BENTS CONSTRUCTED WITH HYBRID REINFORCEMENT

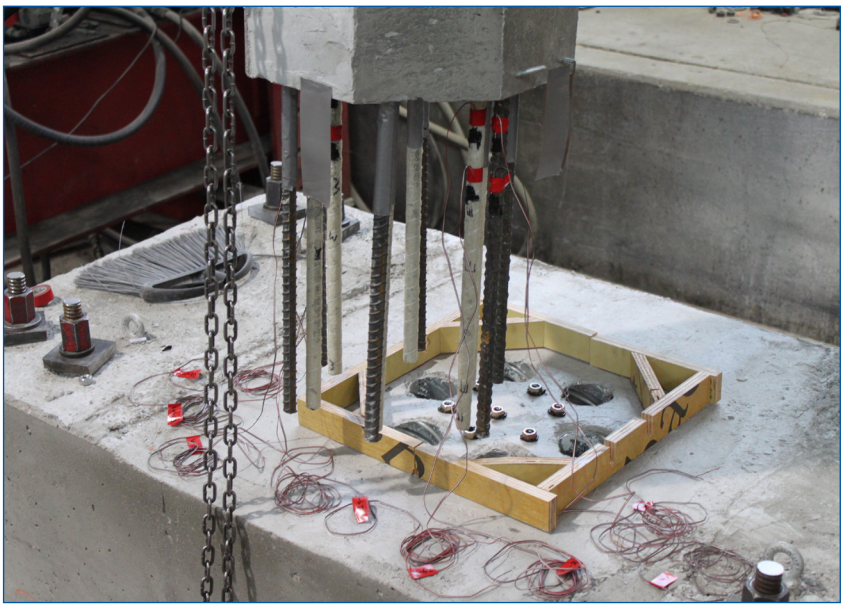

MOUNTAIN-PLAINS CONSORTIUM REGION 8

A University Transportation Center sponsored by the U.S. Department of Transportation serving the Mountain-Plains Region. Consortium members:

Colorado State University
North Dakota State University
South Dakota State University
University of Colorado Denver
University of Denver
University of Utah
Utah State University
University of Wyoming

Technical Report Documentation Page

1. Report No.	2. Government Accession No.	3. Recipient's Catalog No.
MPC-700		

4. Title and Subtitle	5. Report Date
Numerical Analysis of ABC Hybrid Bridge Bents Constructed with Hybrid Reinforcement	June 2024
	6. Performing Organization Code

7. Author(s)	8. Performing Organization Report No.
Chris P. Pantelides Suman Neupane Duc Q. Tran	MPC 24-524

9. Performing Organization Name and Address	10. Work Unit No. (TRAIS)
Department of Civil and Environmental Engineering The University of Utah 110 Central Campus Drive, Room 2000 Salt Lake City, UT 84112	11. Contract or Grant No.

12. Sponsoring Agency Name and Address	13. Type of Report and Period Covered
Mountain-Plains Consortium North Dakota State University PO Box 6050, Fargo, ND 58108	Final Report
	14. Sponsoring Agency Code

15. Supplementary Notes

Supported by a grant from the US DOT, University Transportation Centers Program

16. Abstract

A numerical model simulating the seismic behavior of precast concrete columns confined with glass fiber reinforced polymer (GFRP) spirals and longitudinally reinforced with steel or a combination of steel and GFRP bars was developed using the Open System for Earthquake Engineering Simulation (OpenSees). Four column specimens were tested: two columns with steel and GFRP longitudinal bars (hybrid), and two columns with only steel longitudinal bars (all-steel). All four columns had a double layer of GFRP spiral confinement. One hybrid and one all-steel column were post-tensioned with high-strength steel bars, and carbon fiber-reinforced plastic (CFRP) jackets were applied at the column base for confinement. The columns were connected to footings using grouted duct connections and tested under cyclic loads. A computational modeling strategy is presented to analyze the column-footing connections with steel and FRP composites. The numerical model showed satisfactory agreement with experiments in terms of hysteresis curves, drift ratio at bar fracture, cumulative hysteretic energy (less than 6.0% deviation up to bar fracture), and post-tensioning force prediction (less than 5.0% difference).

Following the successful validation of the numerical model, a similar modeling approach was used to analyze a bent of the Riverdale Bridge using actual dimensions. The aim was to compare the performance of bents reinforced with GFRP bars alongside longitudinal steel bars (hybrid) to those reinforced with steel bars only (all-steel), focusing on the system's ability to dissipate hysteretic energy and self-center. The grouted duct connection was proven effective in resisting seismic lateral forces and bending moments between precast columns and footings in accelerated bridge construction. The hybrid system, combining GFRP bars with longitudinal steel reinforcing bars, demonstrated efficient performance in both self-centering and hysteretic energy dissipation.

17. Key Word	18. Distribution Statement
accelerated bridge construction, construction joints, earthquake resistant structures, reinforcement (engineering)	Public distribution

19. Security Classif. (of this report)	20. Security Classif. (of this page)	21. No. of Pages	22. Price
Unclassified	Unclassified	51	n/a

Numerical Analysis of ABC Hybrid Bridge Bents Constructed with Hybrid Reinforcement

Chris P. Pantelides
Professor

Suman Neupane
Graduate Student

Duc Q. Tran
Graduate Student

Department of Civil and Environmental Engineering
The University of Utah

June 2024

Acknowledgements

The authors acknowledge the financial support provided by the Mountain-Plains Consortium (MPC) under project MPC-700.

Disclaimer

The contents of this report reflect the views of the authors, who are responsible for the facts and the accuracy of the information presented. This document is disseminated under the sponsorship of the Department of Transportation, University Transportation Centers Program, in the interest of information exchange. The U.S. Government assumes no liability for the contents or use thereof.

ABSTRACT

A numerical model simulating the seismic behavior of precast concrete columns confined with glass fiber reinforced polymer (GFRP) spirals and longitudinally reinforced with steel or a combination of steel and GFRP bars was developed using the Open System for Earthquake Engineering Simulation (OpenSees). Four column specimens were tested: two columns with steel and GFRP longitudinal bars (hybrid), and two columns with only steel longitudinal bars (all-steel). All four columns had a double layer of GFRP spiral confinement. One hybrid and one all-steel column were post-tensioned with high-strength steel bars, and carbon fiber-reinforced plastic (CFRP) jackets were applied at the column base for confinement. The columns were connected to footings using grouted duct connections and tested under cyclic loads. A computational modeling strategy is presented to analyze the column-footing connections with steel and FRP composites. The numerical model showed satisfactory agreement with experiments in terms of hysteresis curves, drift ratio at bar fracture, cumulative hysteretic energy (less than 6.0% deviation up to bar fracture), and post-tensioning force prediction (less than 5.0% difference).

Following the successful validation of the numerical model, a similar modeling approach was used to analyze a bent of the Riverdale Bridge using actual dimensions. The aim was to compare the performance of bents reinforced with GFRP bars alongside longitudinal steel bars (hybrid) to those reinforced with steel bars only (all-steel), focusing on the system's ability to dissipate hysteretic energy and self-center. The grouted duct connection was proven effective in resisting seismic lateral forces and bending moments between precast columns and footings in accelerated bridge construction. The hybrid system, combining GFRP bars with longitudinal steel reinforcing bars, demonstrated efficient performance in both self-centering and hysteretic energy dissipation.

TABLE OF CONTENTS

LIST OF FIGURES

LIST OF TABLES

EXECUTIVE SUMMARY

This research focused on establishing a comprehensive numerical model capable of emulating an experimental study conducted on column-to-footing connections with grouted duct connections. The study investigated both all-steel reinforcing details and hybrid reinforcing details, where GFRP bars and mild steel reinforcing bars were used, with and without post-tensioning bars. Once the numerical model successfully predicted the behavior of the half-scale specimens, a parametric study was carried out using the same precast details for an actual bridge bent. The numerical model incorporated various aspects, including modeling of dual longitudinal reinforcement, hybrid reinforcement design, post-tensioning effects, intentional debonding due to GFRP confinement reinforcement, bond-slip behavior, and the plastic hinge length required to estimate the actual seismic properties of the bridge bent. This comprehensive numerical model aimed to accurately predict initial stiffness, maximum lateral load, peak displacement, and hysteretic energy, aligning with the experimental results. The loading and unloading curves from the numerical model matched quite well with the experimental results, suggesting adequate detailing in the numerical model. Results were compared at both the global and local response levels. The cumulative hysteretic energy, a global response parameter, exhibited a maximum difference of 6% between the numerical model and the experiments, indicating that the numerical model satisfied the criteria for global response. For the local response, the reinforcing steel bar fracture was studied, and the numerical model accurately predicted the cycle in which the bar fractured during the experiment, thus verifying the criteria for local response.

Once the numerical model successfully predicted the response of the half-scaled specimens, an actual bridge bent was modeled, and the response was compared between two specimens: one with all-steel reinforcing bars and another with a hybrid arrangement comprising mild steel reinforcing bars and post-tensioning bars. The analysis revealed that the bent with the hybrid specimen and post-tensioning bars exhibited better self-centering performance compared with the all-steel bent with post-tensioning bars. However, the bent with all-steel reinforcement dissipated higher hysteretic energy compared with the hybrid specimen. The choice of reinforcement assignment must be carefully considered based on the design requirements, weighing the importance of superior self-centering capabilities or higher energy dissipation capacity.

Overall, this research developed a comprehensive numerical model that successfully predicted the experimental study, capturing the behavior of column-to-footing connections with grouted duct connections, incorporating various reinforcement configurations, post-tensioning effects, and intentional debonding. The model's ability to predict global and local responses accurately demonstrates its potential for further parametric studies and design optimization of actual precast bridge bents.

LIST OF ACRONYMS

AASHTO	American Association of State Highway and Transportation Officials
ABC	Accelerated Bridge Construction
ACI	American Concrete Institute
ASTM	American Society of Testing and Materials
CFRP	Carbon Fiber-Reinforce Plastic
FHWA	Federal Highway Administration
GFRP	Glass Fiber Reinforced Polymer
GSS	Grouted Splice Sleeve Connectors
CIP	Cast in Place
PCB	Precast Bridge Bent
PT	Post-tensioning
LVDT	Linear Variable Differential Transducer
OpenSees	Open System for Earthquake Engineering Simulation
UDOT	Utah Department of Transportation

1. INTRODUCTION

Accelerated bridge construction (ABC) is a construction method that aims to enhance construction quality and speed, often employing prefabrication techniques to assemble structural elements near the site or at a precast plant, leading to significant time savings compared with traditional methods (Pang et al. 2010; Khaleghi et al. 2012). Seismic design for reinforced concrete (RC) bridges has evolved with the adoption of ABC methods, focusing on connections between prefabricated elements to improve seismic response (Priestley et al. 1996; Haber 2014, 2015; Ameli et al. 2015, 2016; Tazarv and Saiidi 2015, 2016; Ameli and Pantelides 2017). Proper design can mitigate damage in critical areas such as column plastic hinge zones and joints, reducing the risk of reinforcing bar failure and concrete spalling (Kurama et al. 2018; Thapa and Pantelides 2021). Concentrated rotations are vital for tension damage mitigation in precast members, allowing for substantial lateral displacement with minimal tensile stresses. Post-tensioning of columns enhances self-centering, aiding the bridge in returning to its original position after seismic events, thus bolstering seismic resilience.

Grouted ducts represent a connection method utilized in accelerated bridge construction, where galvanized steel ducts are embedded into one precast member and filled with high-strength grout to secure reinforcing dowels from another component. Unlike bar couplers, the grouted duct transfers tensile forces into the surrounding grout, extending beyond the ducts (Barton et al. 2022). This technique, combined with grouted spliced sleeves, is explored to avoid mechanical couplers in critical regions, including plastic hinges or column-to-footing interfaces (Barton et al. 2022). Testing by Matsumoto (2009) and Pang et al. (2010) has been extensive, with preliminary seismic design guidelines already established (Matsumoto 2009; Restrepo et al. 2011). The experiments by Barton et al. (2022) specifically examined intentional debonding of longitudinal bars within columns and footings to enhance displacement ductility and energy absorption during seismic events (Elsayed et al. 2016).

In seismic zones, developing precise models is crucial for predicting bridge performance during earthquakes, particularly since damage is often concentrated around joints and plastic hinge regions. Structural analysis inaccuracies may lead to complete loss of post-tensioning force in numerical models (Erkmen and Schultz 2009). Precast concrete columns with post-tensioned (PT) bars require meticulous design to avoid gaps at joints and ensure effective re-centering (Dangol et al. 2022; Neupane and Pantelides 2024a). Accurate numerical modeling, such as using *Steel4* material with *corotTruss* elements in OpenSees, can replicate cyclic post-tensioning force behavior (Dangol and Pantelides 2023; Neupane and Pantelides 2024b). This modeling assists in determining appropriate initial post-tensioning stress, thus enhancing bridge re-centering and reducing post-earthquake lateral displacement.

Efforts to model the performance of fiber reinforced polymer (FRP) internal reinforcement have intensified with the introduction of FRP composites in bridge construction. Moran et al. (2019) formulated a stress-strain model for analyzing FRP-confined concrete with external FRP jackets, accurately predicting compressive behavior. Sankholkar et al. (2017) assessed the effectiveness of a concrete confinement model with internal GFRP spirals. The goal of these models is to accurately simulate the seismic behavior of GFRP spiral confined concrete columns reinforced with all-steel or hybrid bars, with or without post-tensioning. This will allow modeling of entire bridge bents under typical dynamic loading representative of actual earthquakes.

1.1 Common ABC Connections in Seismic Zones

Using an effective connection type is crucial while building bridges using ABC methods to ensure that joint performance is not compromised under seismic events. The following connection types are commonly used in construction: post-tensioning bars as connectors, grouted duct, grouted splice sleeves, and pocket and socket connections.

1.1.1 Grouted Duct Connection

The column longitudinal steel reinforcement extends into steel corrugated pipes within the cap beam or footing, connected through high-strength grout in grouted duct connections. Previous research by Raynor et al. (2002) highlighted the influence of bond-slip behavior of the reinforcing bar within the grouted duct on structural performance. The presence of ducts exacerbates the bond-slip effect, leading to failure in regions of grouted duct connections (Brenes et al. 2006). To ensure optimal performance, it is recommended to anchor a length from 6 to 10 times the bar diameter (Steuck et al. 2009; Tran and Pantelides 2024a). The recent use of ultra-high-performance concrete has demonstrated improved system performance, making the response comparable to cast-in-place specimens and enhancing displacement and energy dissipation capacity (Tazary and Saiidi 2015).

1.1.2 Pocket Connection

The pocket connection technique involves placing reinforcing bars within a circular corrugated steel duct, thus creating a pocket space that is then filled with normal concrete. This method requires a greater embedment length compared with other connection types. Research conducted by Motaref et al. (2011) on reduced-scale bridge bents indicated that for optimal performance, the embedment length should be 1.5 times the column diameter.

1.1.3 Socket Connection

The socket connection involves connecting a precast concrete column to a spread footing by preparing the footing around the protruding reinforcing bars from the column. Khaleghi et al. (2012) evaluated the performance of this connection and found that a reduced-scale specimen performed better than a monolithic specimen, suggesting its potential use in seismic regions. Since the reinforcing bars protruding from the precast column are concreted together with the spread footing, the failure mechanisms could match those of a cast-in-place specimen (Wang et al. 2019). Performance evaluations of the socket connection have shown that columns can achieve ultimate lateral drifts exceeding 6%, which is higher than the recommended values in design specifications. This suggests that the socket connection can be effectively used in seismically active regions.

1.1.4 Post-tensioning System

Post-tensioning bars serve as connectors between the column and footing interface (Lee and Billington 2009; Mander and Cheng 1997), along with various energy dissipators such as viscous dampers, buckling restrained braces (BRBs), dog-bone milled steel bars, and stretch length anchors (SLAs) (Lee et al. 2001; Guerrini et al. 2014; Thapa and Pantelides 2021; Dangol and Pantelides 2022; and Neupane and Pantelides 2024b). Unlike traditional connections, post-tensioning elements only traverse the column-to-footing/cap beam interface, eliminating reinforcing bars passing through them. This setup induces rocking behavior, minimizing permanent lateral deformation, and enhancing self-centering capability, making it a popular choice in recent years.

1.1.5 Grouted Spliced Sleeves (GSS)

GSS connections are commonly employed in accelerated bridge construction, utilizing grouted splice sleeves as connectors between factory and field dowels. There are two methods of using GSS: fastened grouted spliced sleeve (FGSS) and grouted-grouted spliced sleeve (GGSS). In this study, GGSS connectors were utilized, recessed beneath the column-to-footing interface within the footing. Bond stress between reinforcing bars and high-strength grout facilitates the transfer of compressive and tensile forces during cyclic loading. GGSS reinforcing bars require shorter embedment lengths (25% of standard specifications) due to their strong confinement, which prevents splitting failure. Figure 1.1 illustrates typical GSS connections.

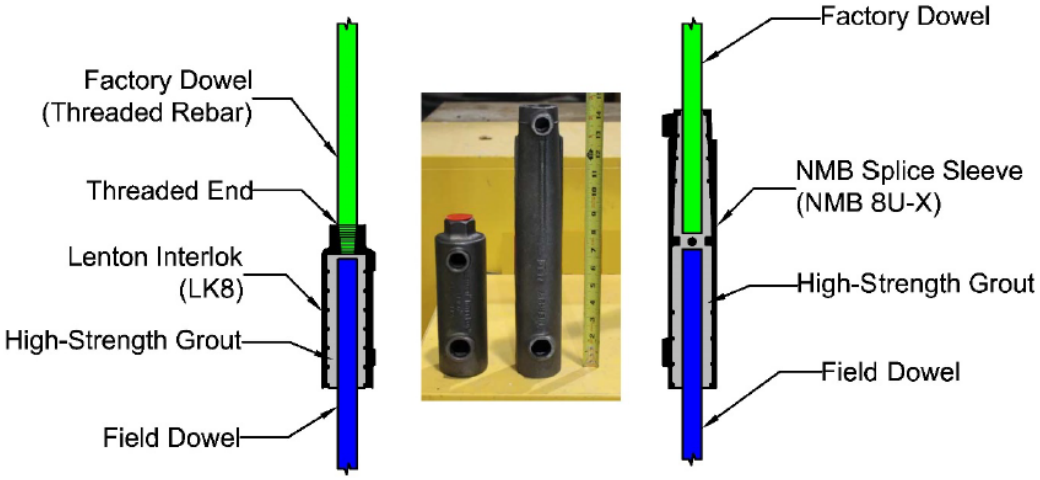

Figure 1.1 Two types of grouted splice sleeve connectors

2. DESIGN AND CONSTRUCTION OF BRIDGE BENT

Four column-to-footing specimens were constructed for cyclic experiments, each consisting of a column and a footing. Table 2.1 outlines the test matrix. All columns were equipped with two layers of internal longitudinal bars; the outer layer of the longitudinal bars was mild steel bars. This outer layer allows the steel bars to yield, enhancing displacement ductility and preventing sudden structural failure. The inner layer of longitudinal bars included either GFRP bars, which classifies the columns as hybrid (HYB), or mild steel bars, which classifies them as all-steel (STL). Two columns were constructed without post-tensioning (Figure 2.1), while the other two had embedded PVC pipes (Figure 2.2) for installation of post-tensioning bars. After assembly with grouted ducts, one hybrid and one all-steel specimen were post-tensioned using high-strength steel bars, designated as PT-HYB and PT-STL, respectively. The elastic properties of GFRP reinforcement and post-tensioning forces from the PT bars enhance the system's re-centering capability.

Double layers of confining GFRP spirals were installed at 51 mm spacing with a 13M GFRP bar diameter, as shown in Figure 2.1, to compensate for the lower modulus of elasticity of GFRP bars (Tran and Pantelides 2024a) and to improve corrosion resistance (Pantelides et al. 2013). The columns had an octagonal cross-section and were 2.49 m long, reinforced with twelve 19M longitudinal bars in two layers. These bars extended beyond the column ends and were embedded in galvanized ducts in the footing using high-strength grout. The concrete cover for both columns was 25 mm. The longitudinal reinforcement ratio was 2.50% for the all-steel column (STL); for the hybrid column the ratio was 1.25% for steel and 1.25% for GFRP.

Each column used two 1,034 MPa 25M all-thread high-strength steel bars for post-tensioning, as depicted in Figure 2.2; the selected post-tensioning reinforcement ratio was 0.75%. The PT bar properties provided by the manufacturer were as follows: ultimate tensile strength of 567 kN and a yield capacity of 454 kN. Proper initial post-tensioning force is crucial to keep the PT bars within the elastic range, with each PT bar initially tensioned to 191 kN. Two layers of CFRP wrap were applied to the columns of specimens PT-HYB and PT-STL for a height of 610 mm at the column base to confine the concrete under high post-tensioning forces, as shown in Figure 2.2. The four specimens can be summarized as follows:

1. Specimen with all steel reinforcing bars in two layers with GFRP spirals (STL)
2. Specimen with inner layer GFRP bars and outer layer steel reinforcing bars with GFRP spirals (HYB)
3. Post-tensioned specimen with all steel reinforcing bars in two layers with GFRP spirals (PT-STL)
4. Post-tensioned specimen with inner layer GFRP bars and outer layer steel reinforcing bars with GFRP spirals (PT-HYB)

The reinforcing bars extending from the column were intentionally debonded into two distinct groups. For columns HYB and STL, without post-tensioning (Figure 2.1), all intentional debonding occurred within the footing, starting from its top, with a debonding length of eight times the bar diameter (8db) or 152 mm inside the footing. For columns PT-HYB and PT-STL with post-tensioning (Figure 2.2), intentional debonding occurred within both the column and footing, with 152 mm debonded in the footing and 152 mm in the column, totaling a debonded length of 304 mm. Footing details, including overall dimensions, mild steel reinforcement details, and six grouted ducts, are provided in Figure 2.3. More details on the construction of the column-to-footing specimens are available elsewhere (Tran and Pantelides 2024a; Tran and Pantelides 2024b).

Table 2.1 Test matrix

Column Designation	Longitudinal Reinforcement	Spiral Reinforcement	Bar Debonded Length in Ducts (mm)	Bar Debonded Length in Columns (mm)
HYB	6-19M Steel (Outer) 6-19M GFRP (Inner)	2 layers of 13M GFRP	152	0
STL	6-19M Steel (Outer) 6-19M Steel (Inner)	2 layers of 13M GFRP	152	0
PT-HYB	6-19M Steel (Outer) 6-19M GFRP (Inner)	2 layers of 13M GFRP	152	152
PT-STL	6-19M Steel (Outer) 6-19M Steel (Inner)	2 layers of 13M GFRP	152	152

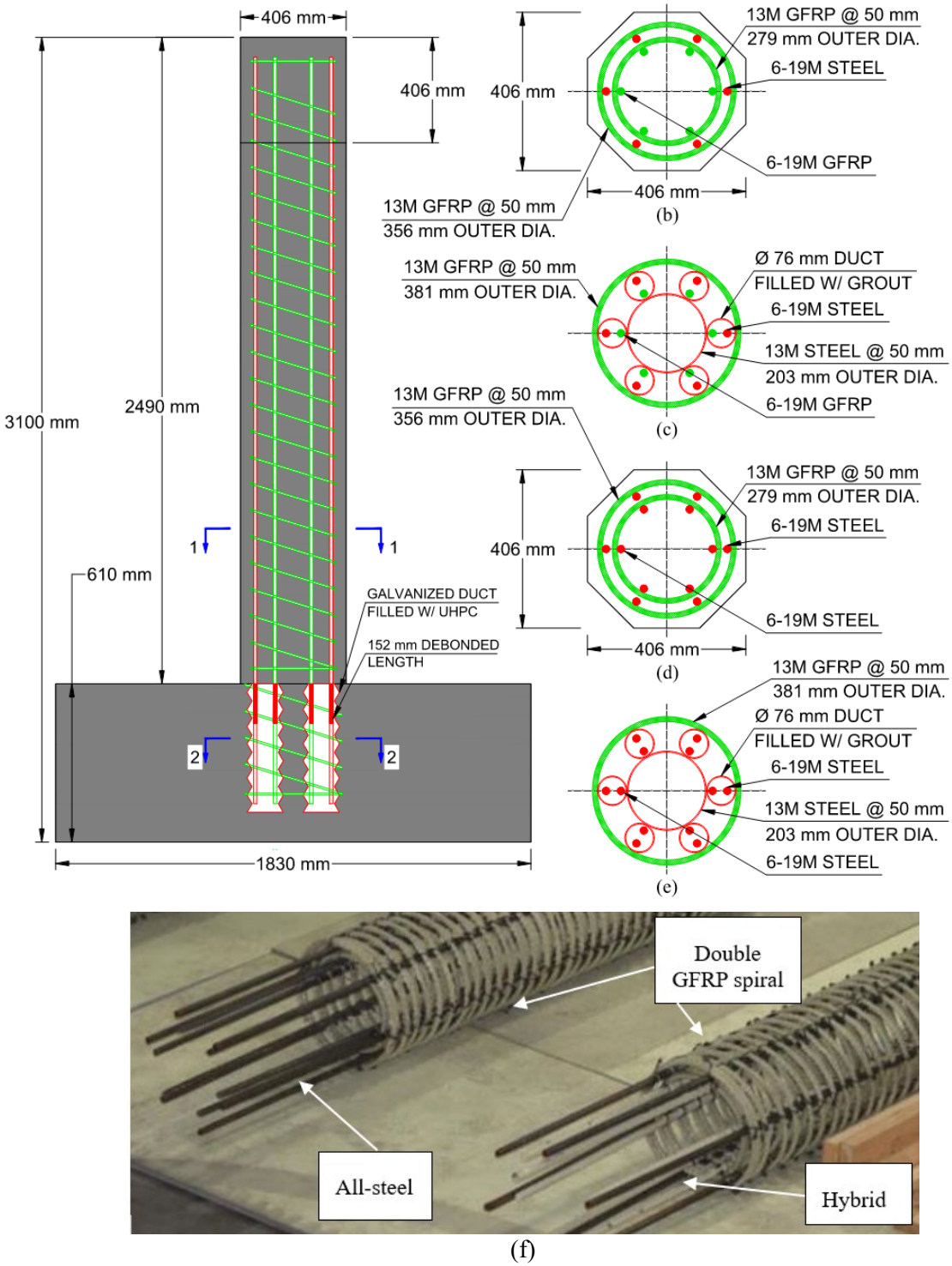

Figure 2.1 All-steel and hybrid column details: (a) side view; (b) section 1-1 HYB column; (c) section 2-2 HYB column; (d) section 1-1 STL column; (e) section 2-2 STL column; and (f) column reinforcement

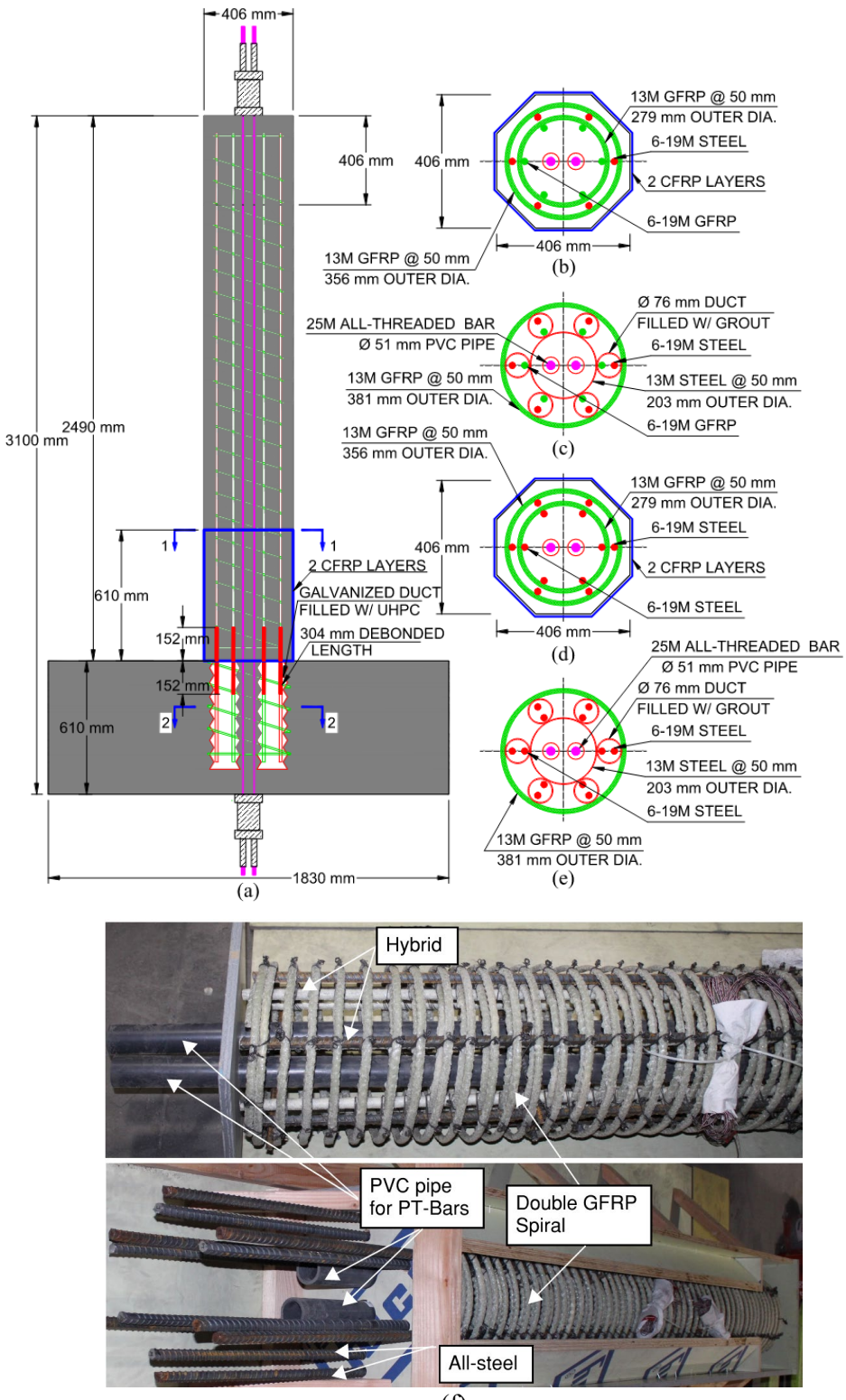

Figure 2.2 Post-tensioned column details: (a) side view; (b) section 1-1 PT-HYB column; (c) section 2-2 PT-HYB column; (d) section 1-1 PT-STL column; (e) section 2-2 PT-STL column; and (f) column reinforcement

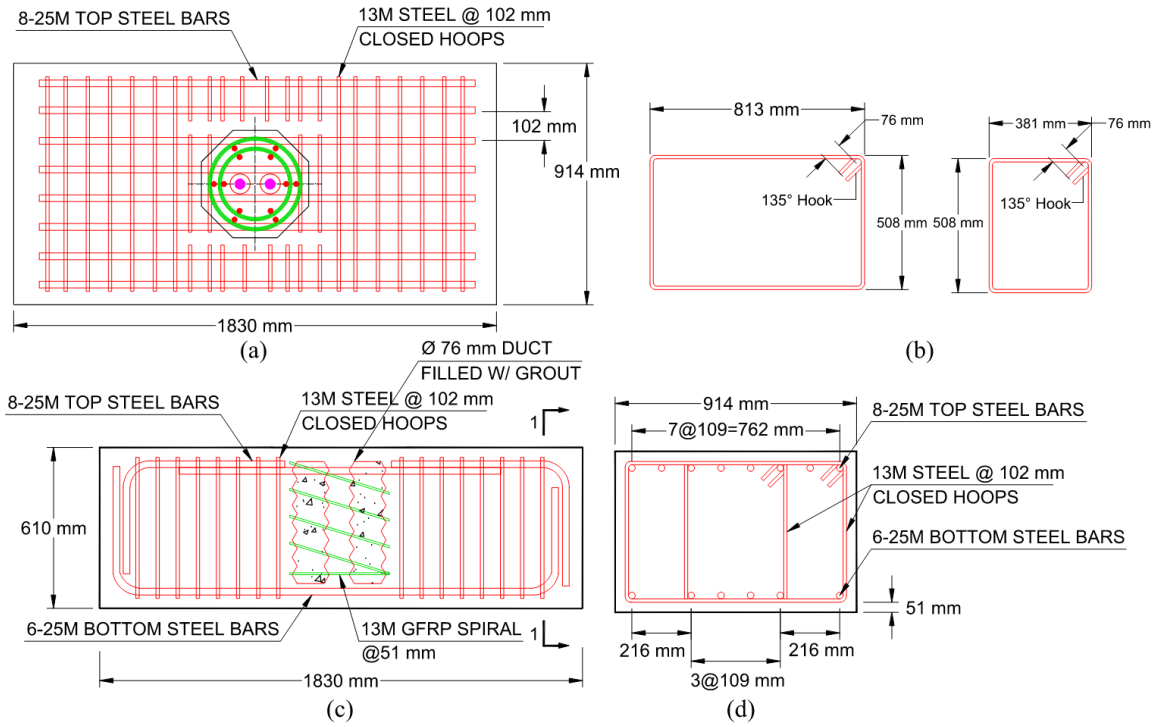

Figure 2.3 Footing details: (a) top view; (b) side view; (c) section 1-1; and (d) footing reinforcement

3. TEST SETUP AND EXPERIMENTAL RESULTS

3.1 Test setup

The cantilever column was connected to the footing, which was fixed to the base of the strong floor at the Structures Laboratory of the University of Utah. Threaded bars were used to fix the footing to the strong floor using wide flange steel I-beams. A hydraulic actuator was used to apply the cyclic quasi-static cyclic load at the top of the column. An 800 kN servo-controlled actuator with a 610 mm stroke was used to apply the lateral cyclic load, as shown in Figure 3.1(a, b). An axial load equal to 6.0% of the column axial compression capacity was applied to simulate the weight of the bridge superstructure. The loading protocol used in the experiments is shown in Figure 3.1(e). The displacement rate of the cyclic lateral load was 31 mm/min for drift ratios up to 3.0% and was increased to 102 mm/min for drift ratios above 4.0%. A detail of the two load cells, located at the bottom of the footing, used to measure the post-tensioning forces is shown in Figure 3.1(d). Strain gauges were provided to measure strain in the reinforcing bars during cyclic loading; string pots were used to measure the lateral displacement of the column; and linear variable displacement transducers (LVDTs) were used to measure column rotation and curvature at several locations. The typical setup of the experimental study is shown in Figure 3.1(c).

3.2 Test Results

The columns without post-tensioning reached a final drift ratio of 11.0%, exhibiting concrete spalling in the plastic hinge area. In the hybrid column (HYB), the initial failure was a GFRP bar fracture in compression, followed by fracture of two steel bars in tension and two turns of the outer GFRP spiral in tension, while the inner GFRP bars remained intact. The peak lateral load recorded was 120 kN, with a corresponding lateral displacement of 197 mm at a 9.0% drift ratio. For the all-steel (STL) column, two steel bars and two turns of the outer GFRP spiral fractured in tension at an 11.0% drift ratio. This column exhibited a lateral load capacity of 130 kN at a 123 mm lateral displacement during the 6.0% drift ratio. The hysteresis of the HYB and STL columns is depicted in Figure 3.2(a), demonstrating that the longitudinal GFRP bars enhance self-centering capacity.

The post-tensioned columns reached a final drift ratio of 12.0%, with the CFRP jacket fracturing at the column-to-footing interface. In the hybrid post-tensioned column (PT-HYB), concrete spalling occurred above the CFRP jacket, and a steel bar fractured in tension. This column achieved a lateral load capacity of 193 kN, corresponding to a 221 mm lateral displacement at a 10.0% drift ratio. Conversely, the all-steel post-tensioned column (PT-STL) experienced fracture of two longitudinal steel bars in tension, maintaining high stiffness until the 6.0% drift ratio and achieving a plateau at higher drift ratios. The lateral load capacity for this column was 184 kN, with a 155 mm displacement at a 7.0% drift ratio. Figure 3.2(b) presents the hysteresis curves of the two post-tensioned columns. During the PT-HYB test, the peak post-tensioning force reached 398 kN, equivalent to 88% of the yield limit; while in the PT-STL test, it reached 413 kN, or 91% of the yield limit. The impact of post-tensioning is evident in the enhanced re-centering compared with the non-post-tensioned columns shown in Figure 3.2(b), and the longitudinal GFRP bars further improve self-centering capacity. Table 3.1 shows the summary of the experimental results and gives the value for ultimate drift ratio, ductility, initial stiffness, and total hysteretic energy for all four experimental specimens.

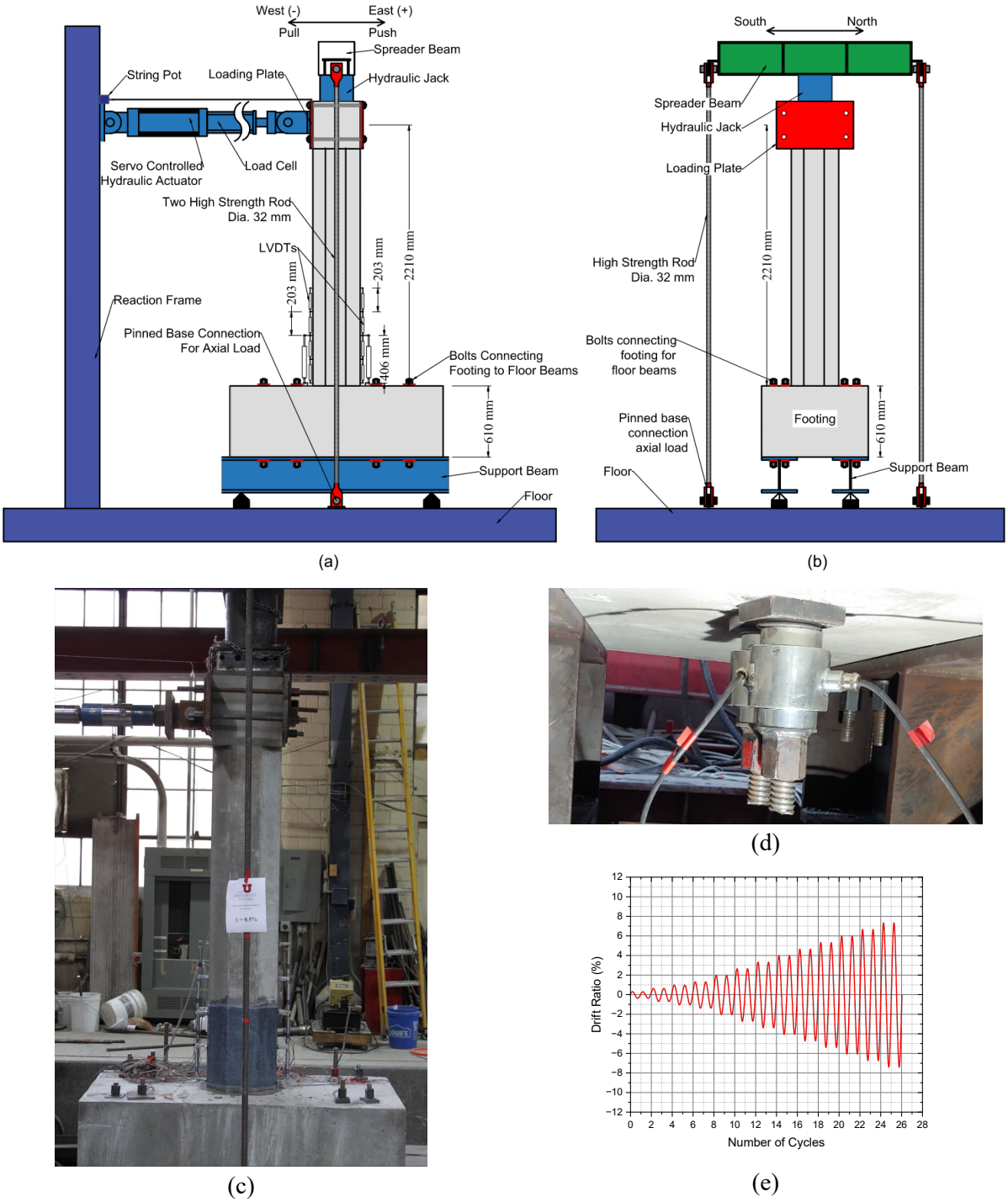

Figure 3.1 Test setup: (a) testing scheme front view; (b) testing scheme side view; (c) experimental setup; (d) load cell setup; and (e) loading protocol

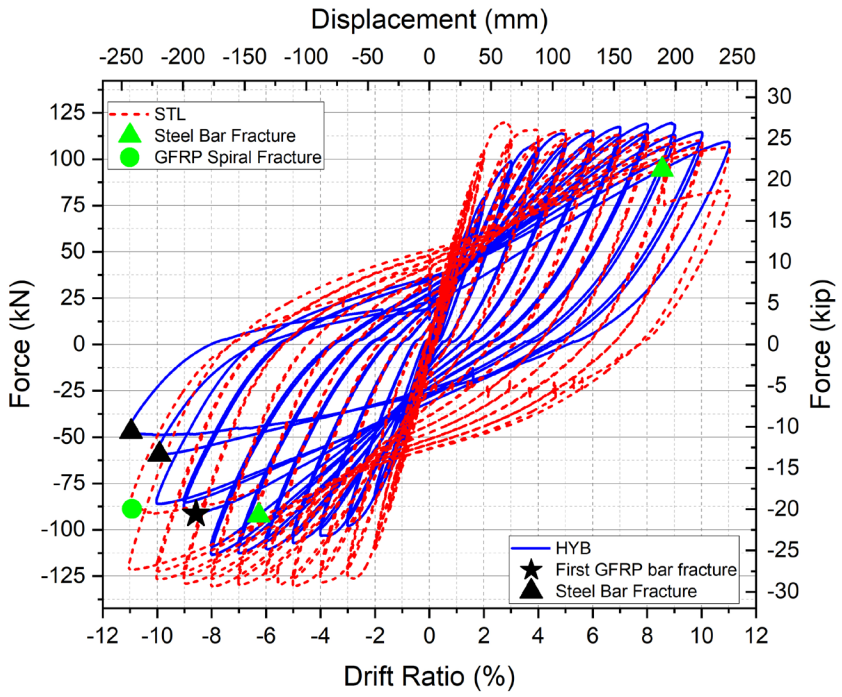

(a)

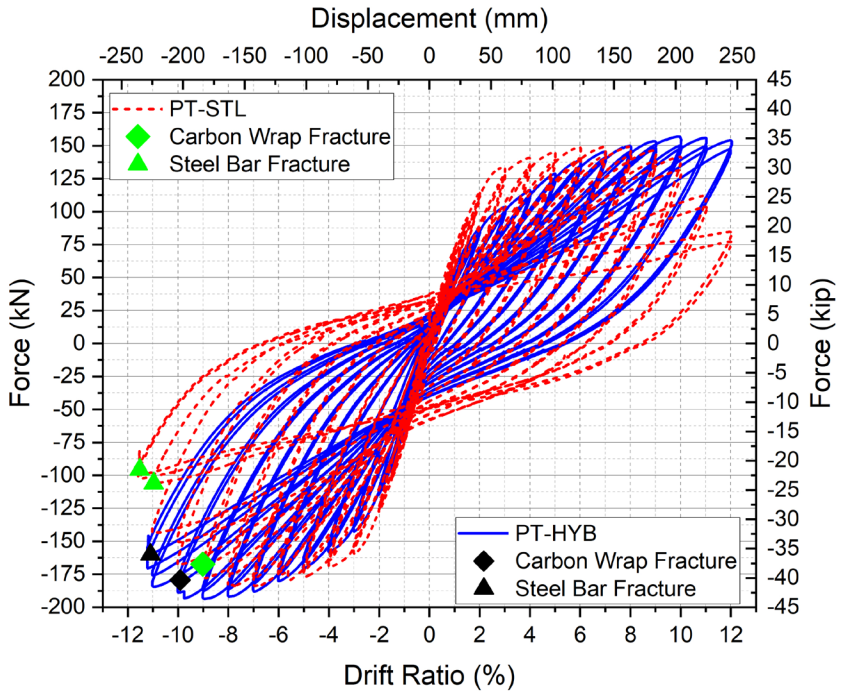

(b)

Figure 3.2 Experimental hysteresis comparison: (a) HYB and STL columns; and (b) post-tensioned PT-HYB and PT-STL columns

Table 3.1 Summary of experimental results

Parameters	**STL**	**HYB**	**PT-STL**	**PT-HYB**
Drift ratio at test termination (%)	11.0	11.0	12.0	12.0
Initial stiffness (kN/mm)	3.64	2.77	3.40	2.94
Ductility	5.5	4.0	N/A	N/A
Hysteretic energy (kN-m)	413	188	347	248

4. NUMERICAL MODEL

4.1 Numerical Modeling

Nonlinear analysis is a valuable tool for designing and assessing the seismic performance of bridges. The numerical analysis objective is to develop a predictive model capable of accurately simulating the seismic behavior of GFRP-confined columns reinforced with all-steel or hybrid bars, with or without post-tensioning. In large earthquakes, structural components often exhibit nonlinear material behavior. This phenomenon can be effectively modeled using distributed plasticity or force-based beam-column elements with fiber sections. The overall structural response is obtained through numerical integration along the element, providing a comprehensive understanding of failure mechanisms.

Reliable models are essential for designing, analyzing, and predicting the seismic response of post-tensioned precast and hybrid bridge columns. There are significant challenges in analyzing the response of the hybrid arrangement of steel and GFRP longitudinal bars in combination with post-tensioning. These challenges include addressing the nonlinear behavior of GFRP-confined reinforced concrete columns, combining the attributes of hybrid steel and GFRP vertical reinforcement including bond-slip, and understanding the joint behavior in post-tensioned systems. GFRP longitudinal bars and GFRP spirals are relatively new materials for precast concrete column construction. Accurate modeling of the post-tensioned high-strength steel bars is important for obtaining accurate numerical results.

4.2 Description of Computational Model

The Open System for Earthquake Engineering Simulation (OpenSees), an open-source software framework for seismic simulation using finite element methods, is used to create a two-dimensional (2D) model of a cantilever column configuration (McKenna et al. 2010). This model comprises a comprehensive framework encompassing material models and the ability to implement cyclic loading, thus enabling modeling of column-to-footing connections (Tazarv and Saiidi 2016; Ameli and Pantelides 2017; Zhuo et al. 2019; Shrestha and Pantelides 2024). The primary purpose of the model is to ascertain the influence of the parameters associated with the GFRP and steel reinforcing bars employed in the plastic hinge length region of all four columns, along with the effect of post-tensioning. This analytical work aims to create models capable of predicting the performance of hybrid, all-steel, and post-tensioned bridge columns using OpenSees.

4.3 Material Model

4.3.1 Concrete

The concrete in the columns has two distinct properties based on location: core concrete and cover concrete. Since GFRP spirals confine the concrete section as transverse reinforcement, the core concrete exhibits a higher compressive strength (Sankholkar et al. 2017). The cover concrete is unconfined, and its parameters were determined using the compressive strength obtained from compression cylinder tests. The *UniaxialMaterial Concrete04* material model, available in OpenSees, was utilized to model the unconfined concrete properties using Mander's model (Mander et al. 1988), as illustrated in Figure 4.1. For columns externally wrapped with two CFRP layers, the cover concrete is confined by the CFRP jacket, and it was modeled using the confinement model by Moran et al. (2019). Core concrete confined with GFRP spirals was modeled using the model by Sankholkar et al. (2017). Core concrete confined by both external CFRP jackets and GFRP spirals was modeled using a combination of the Sankholkar et al. (2017) model for GFRP spirals and the Moran et al. (2019) model for CFRP jackets. On test day, the concrete compressive strength from cylinder tests was 55 MPa.

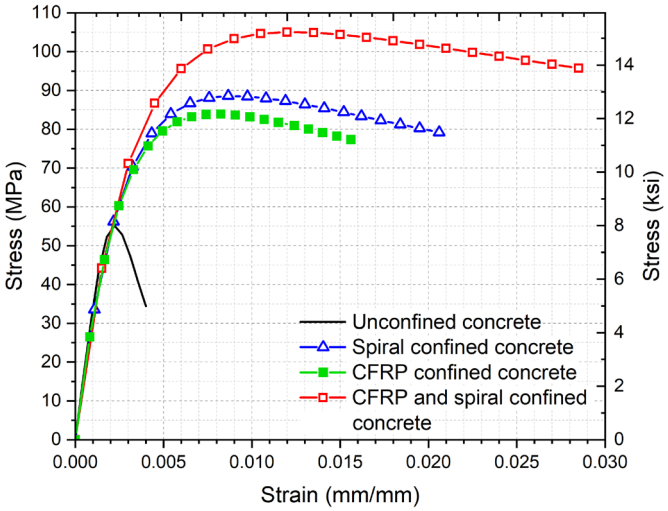

Figure 4.1 Concrete material model

4.3.2 Mild Steel Reinforcing Bar

The reinforcing bars were modeled using the *ReinforcingSteel* material available in OpenSees (Kunnath et al. 2009). This uniaxial material incorporates reinforcing bar properties, including stress-strain performance under lateral loading. The reinforcing steel was modeled as an isotropic strain-hardening material, accounting for yield strength, ultimate strength, modulus of elasticity, tangent modulus at initial strain hardening, and strain corresponding to hardening. Fatigue parameters were based on the Coffin-Manson equation (Manson 1965). The reinforcing bar buckling model was derived from Dhakal and Maekawa (2002). The original reinforcing bar properties suggested by Haber et al. (2013) were used for regions outside the plastic hinge, as shown in Figure 4.2. However, within the plastic hinge region, the material properties were modified due to intentional debonding and bar bond-slip, as discussed subsequently.

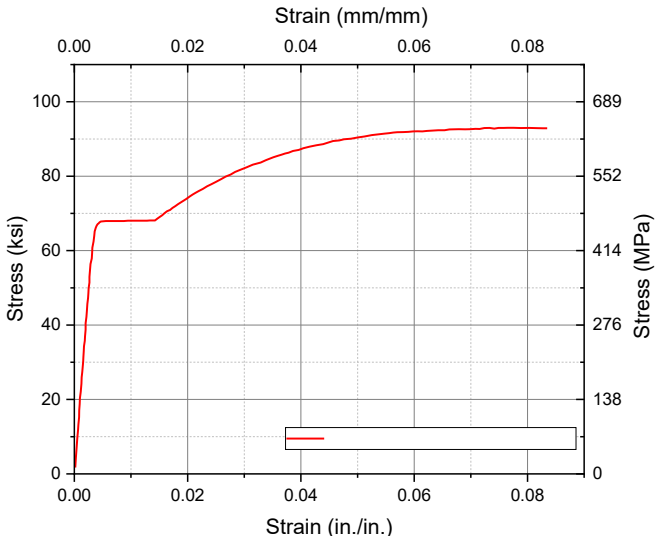

Figure 4.2 Original reinforcing bar properties (Haber et al. 2013)

4.3.3 Low Cycle Fatigue

Reinforcing bars experience bending and straightening due to repetitive cyclic loading, which leads to fatigue and can cause fractures, particularly under high strain conditions. The $ReinforcingSteel$ material model addresses low-cycle fatigue by integrating the Coffin-Manson expression (Manson 1965). Kunnath et al. (2009) introduced a cumulative damage rule that can be used alongside the Coffin-Manson model to forecast fatigue during cyclic degradation.

$$\varepsilon^p = C_f\left(2N_f\right)^{-\alpha} \tag{1a}$$

$$D_f = \frac{1}{\sum_{i=1}^{n}(2N_f)_i} \tag{1b}$$

where, ε^p is the plastic strain, C_f and α are material constants equal to 0.26 and 0.506, respectively, and $2N_f$ is the number of half cycles to failure. Values of these parameters are altered to align them with experimental results (Mazzoni et al. 2006).

4.3.4 Bar Bond-slip and Debonding Model

To assess the bond-slip effect, three factors must be considered: slip between the grout and reinforcing bar, slip effects due to intentional debonding of reinforcing bars, and the combined impact of bar-slip and intentional debonding. Reinforcing bars undergoing bond slip experience changes in strain within the debonded area. The modified modulus of these bars, as a result of this effect, was determined through experimental findings (Tazarv and Saiidi 2015). Tazarv and Saiidi (2015) developed a constitutive bond-slip model for reinforcing bars with adequate anchorage length, incorporating an initial elastic region and adjusted properties of the bars in that region. These elastic properties apply where slippage occurs, which happens between the grout and reinforcing bar, known as rebar bond-slip, and at the intentional debonding region.

When lateral load is applied to the system, steel reinforcing bars and GFRP bars start slipping from the concrete; this phenomenon needs to be incorporated in the numerical model to accurately predict the experimental behavior. The bond-slip effect for steel reinforcing bars is calculated considering the slip between steel bars and grout; the grouted ducts inside the footing also experience bond slip with the footing concrete. Expressions from the literature are used to calculate the bond-slip effect of grouted ducts and steel reinforcing bars (Tazarv and Saiidi 2015). In addition to bond-slip, the intentional debonding provided to the GFRP and steel bars must be considered since it delays bar fracture until higher drift ratios are reached (Neupane et al. 2023). The numerical model incorporates both the bond-slip behavior of reinforcing bars (Tazarv and Saiidi 2015) and the intentional debonding effect of reinforcing bars (Neupane et al. 2023). From these expressions, the pseudo modulus of elasticity for the steel reinforcing bars was calculated as 124 GPa. The pseudo modulus of elasticity was applied within the plastic hinge, while the actual steel bar properties were utilized outside the plastic hinge. The parameters used to calculate the pseudo modulus, along with the values of both the pseudo modulus and the actual modulus, are presented in Table 4.1. The stress-strain properties for both pseudo and actual steel reinforcing bars are shown in Figure 4.3.

Table 4.1 Properties from $ReinforcingSteel$ and GFRP bond-slip and debonding calculation

Properties	Parameters used in the Model	
	Steel Reinforcement	**GFRP bar**
Embedment length ($\boldsymbol{l_{emd}}$)	534 mm	534 mm
Duct diameter ($\boldsymbol{d_d}$)	76 mm	76 mm
Bar diameter ($\boldsymbol{d_b}$)	19 mm	19 mm
Concrete strength ($\boldsymbol{f'_c}$)	55 MPa	55 MPa
Grout strength ($\boldsymbol{f'_{grout}}$)	83 MPa	83 MPa
Duct bond- slip stiffness ($\boldsymbol{k_d}$)	532 kN/mm	532 kN/mm
Bar bond-slip stiffness ($\boldsymbol{k_b}$)	42 kN/mm	42 kN/mm
Actual modulus ($\boldsymbol{E}$)	200 GPa	41 GPa
Pseudo Modulus ($\boldsymbol{E_{mod}}$)	124 GPa	20 GPa
Yield stress ($\boldsymbol{f_y}$)	470 MPa	N/A
Tensile strength ($\boldsymbol{f_{ult}}$)	650 MPa	690 MPa

The numerical model also contains an actual GFRP bar outside the plastic hinge and a pseudo GFRP bar inside the plastic hinge region. The pseudo GFRP bar and actual GFRP reinforcing bar properties are calculated to model the effects of bond-slip and GFRP bar intentional debonding. Modified strain due to bond-slip for any given stress can be calculated considering both GFRP bar slip and grouted duct slip. Experimental results from pullout tests for 19M bars demonstrated this behavior (Tran and Pantelides 2024a); however, the number of tests was not statistically significant to propose new equations, hence the expressions from Tazarv and Saiidi (2015) were used for GFRP bond-slip calculations. The modified strain corresponding to any stress for GFRP bars can be found as:

$$\varepsilon'_{bond-slip} = \varepsilon_s + \frac{\left(\frac{F}{k_d}+\frac{F}{k_b}\right)}{L_{emd}} \quad (2)$$

$$k_d = 11310 d_d \sqrt{f'_c} \quad (3)$$

$$k_b = 2920 d_b \sqrt{f'_{grout}} \quad (4)$$

where, $\varepsilon'_{bond-slip}$ is the modified strain after considering the bar and duct slip, ε_s is the normal strain relationship for the longitudinal GFRP bar, k_d is the duct bond-slip stiffness, k_b is the longitudinal bar bond-slip stiffness, l_{emd} is the embedment length, d_d is the diameter of the duct, d_b is the diameter of the longitudinal bar, f'_c is the compressive strength of the concrete, and f'_{grout} is the compressive strength of the grout. Table 4.1 lists the properties used for the GFRP bond-slip calculation and the value of the pseudo modulus of the GFRP bar used in the numerical model.

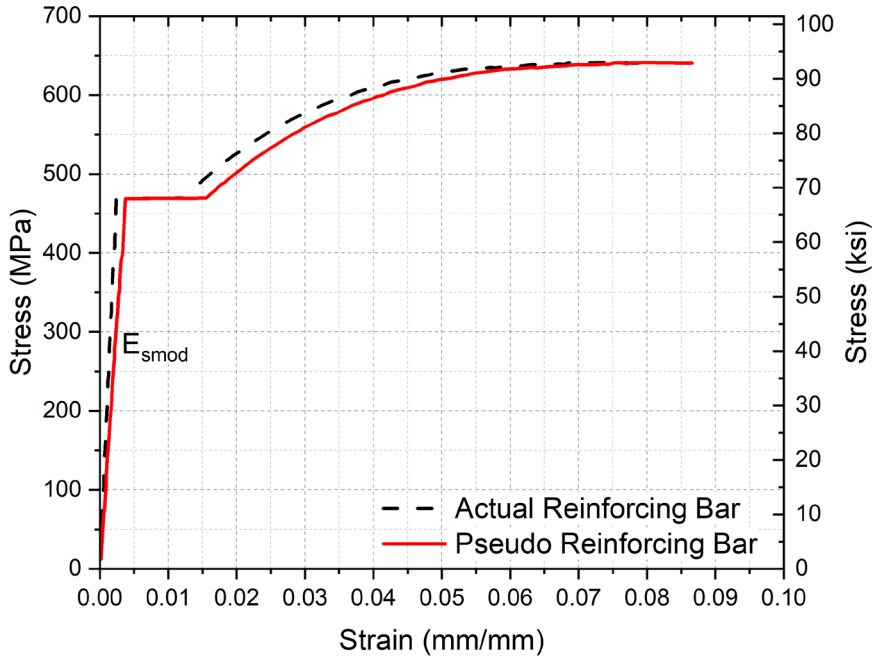

Figure 4.3 Steel reinforcing bar model with and without considering bond-slip and intentional debonding

The effect of intentional debonding of longitudinal GFRP bars is also considered in the numerical model. The model by Neupane et al. (2023) is used to consider the effect of intentional debonding. Due to intentional debonding, extra longitudinal strain will develop in the GFRP bars. For steel bars within the elastic range of the material, the additional strain due to debonding is assumed to be one-half of the tensile strain at the same stress. Computation of the additional strain due to debonding of GFRP bars was calibrated from the hysteretic response of the numerical model, keeping other parameters constant. GFRP bars have elastic material properties up to fracture; hence, Eq. (4) can be used to account for debonding effects in which the additional strain due to debonding is assumed as one-half of the elastic strain. For any applied stress in the GFRP bar, the additional strain due to intentional debonding is:

$$\varepsilon'_{debonding} = \frac{\varepsilon_{elastic}}{2} \quad (5)$$

Thus, the total effect of bond-slip and debonding for a given applied stress ($f_{elastic}$) to the GFRP bar is found as:

$$\varepsilon_{mod} = \varepsilon'_{bond-slip} + \varepsilon'_{debonding} \quad (6)$$

For a given applied stress to the GFRP bar, the modified strain ε_{mod} is calculated. Once the stress-strain curve of GFRP bars is obtained, the modulus of elasticity, including intentional debonding and bond-slip, gives the pseudo modulus of GFRP bars. The actual GFRP bar stress-strain properties outside the plastic hinge and the pseudo GFRP properties inside the plastic hinge are illustrated in Figure 4.4. The tensile strength of the GFRP bars was provided by the manufacturer as 690 MPa and the modulus of elasticity as 41 GPa. The compressive strength of GFRP bars was conservatively estimated as 49% of the tensile strength using the material's elastic modulus, as shown in Figure 4.4 (Wright and Pantelides 2021). The pseudo modulus of GFRP bars was equal to 20 GPa; this was determined from the slope of the stress-strain curve with bond-slip and intentional debonding. The actual modulus of elasticity of the GFRP bars is used to model the GFRP bar outside the plastic hinge region. The material for GFRP bars is modeled as *elastic* material properties.

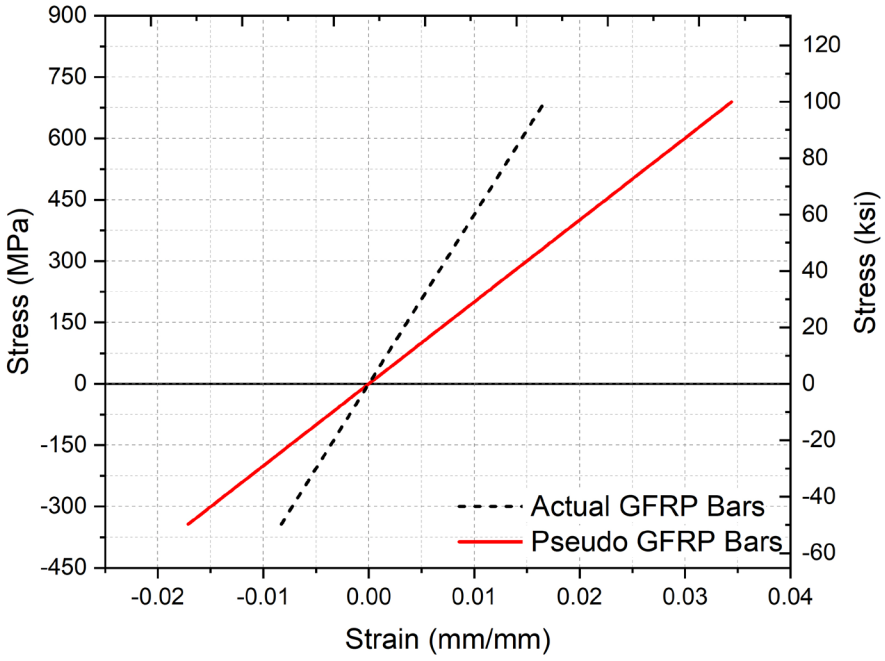

Figure 4.4 Fiberglass reinforcing bar material model with and without considering bond-slip and intentional debonding

4.3.5 Bar Buckling Model

Buckling of reinforcing bars is modeled using the approach proposed by Dhakal and Maekawa (2002). This buckling model requires two parameters: the slenderness ratio and an amplification factor. The value of the amplification factor depends on whether the material exhibits linear strain hardening behavior or elastic perfectly plastic material behavior. In the general case, the material is assumed to be a linear strain hardening material, and the amplification factor is taken as 1.0 (Dhakal and Maekawa 2002).

4.3.6 Post Tensioning Bar Model

The stress-strain curve of the PT bar is shown in Figure 4.5. The *UniaxialMaterial Steel4* model was used to define tensile stress-strain behavior for the PT bars with initial stress accommodation. PT bar properties include yield stress of 827 MPa, modulus of elasticity of 186 GPa, hardening ratio of 0.095, transition control parameter at 16.0, constant parameters r1 and r2 at 0.9 and 0.1, respectively, ultimate tensile stress of 1,034 MPa, and transition control parameter for kinematic hardening to plastic asymptote at 2.0. Isotropic hardening is excluded due to non-uniform yield surface expansion post-yield stress. The *corotTrussElement* was used to model the post-tensioning bars with *Steel04* material properties (Dangol and Pantelides 2023; Neupane and Pantelides 2024a). The *corotTrussElement* considers the nonlinear geometry of the material that occurs during column bending. Nonlinear transformation is used for PT bars due to geometric nonlinearity arising from the elongation of PT bars during application of the lateral load.

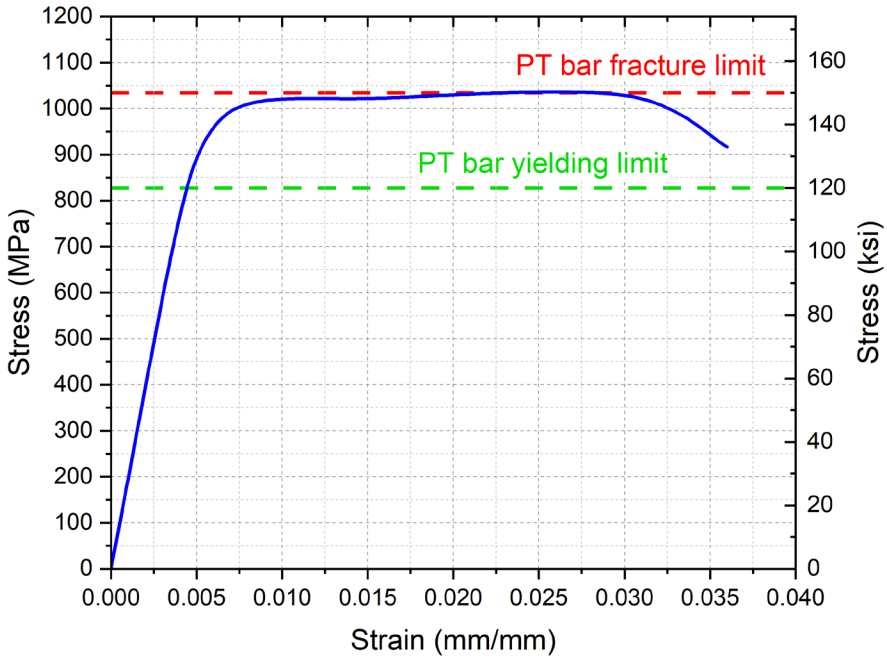

Figure 4.5 Material properties of post tensioning bars

4.4 Model Layout

An OpenSees 2D numerical model of a single-column pier was formulated using a *force-based BeamColumnElement*, as described by Scott (2007). This element incorporates various numerical integration points coupled with a plastic hinge length. Regarding the presence of PT bars, *elasticBeamColumnElement* was used to connect the PT bars modeled as *corotTrussElement*.

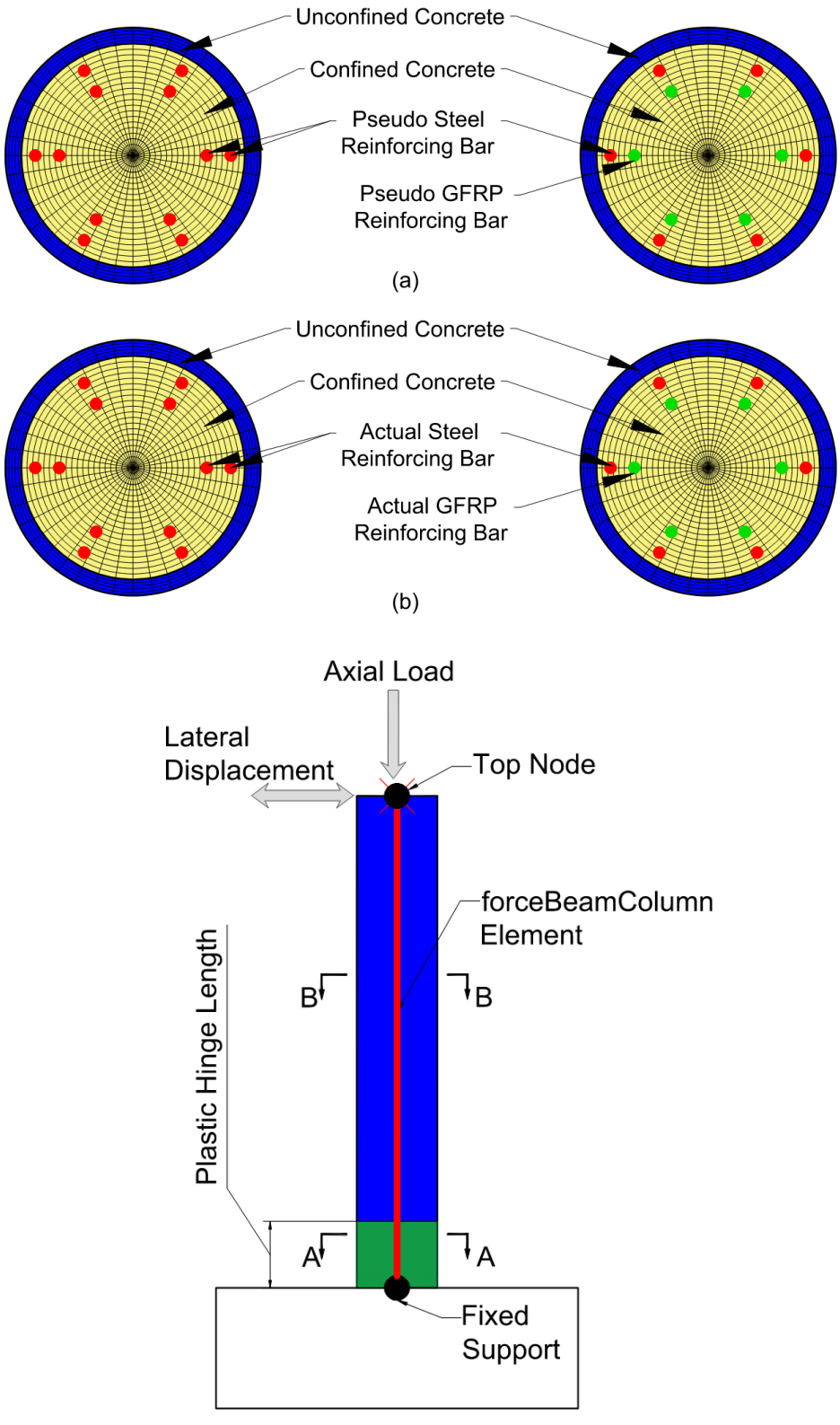

Figure 4.6 All-steel and hybrid column cross-section and numerical model layout: (a) inside plastic hinge region (section A-A); (b) outside plastic hinge region (section B-B); and (c) model layout

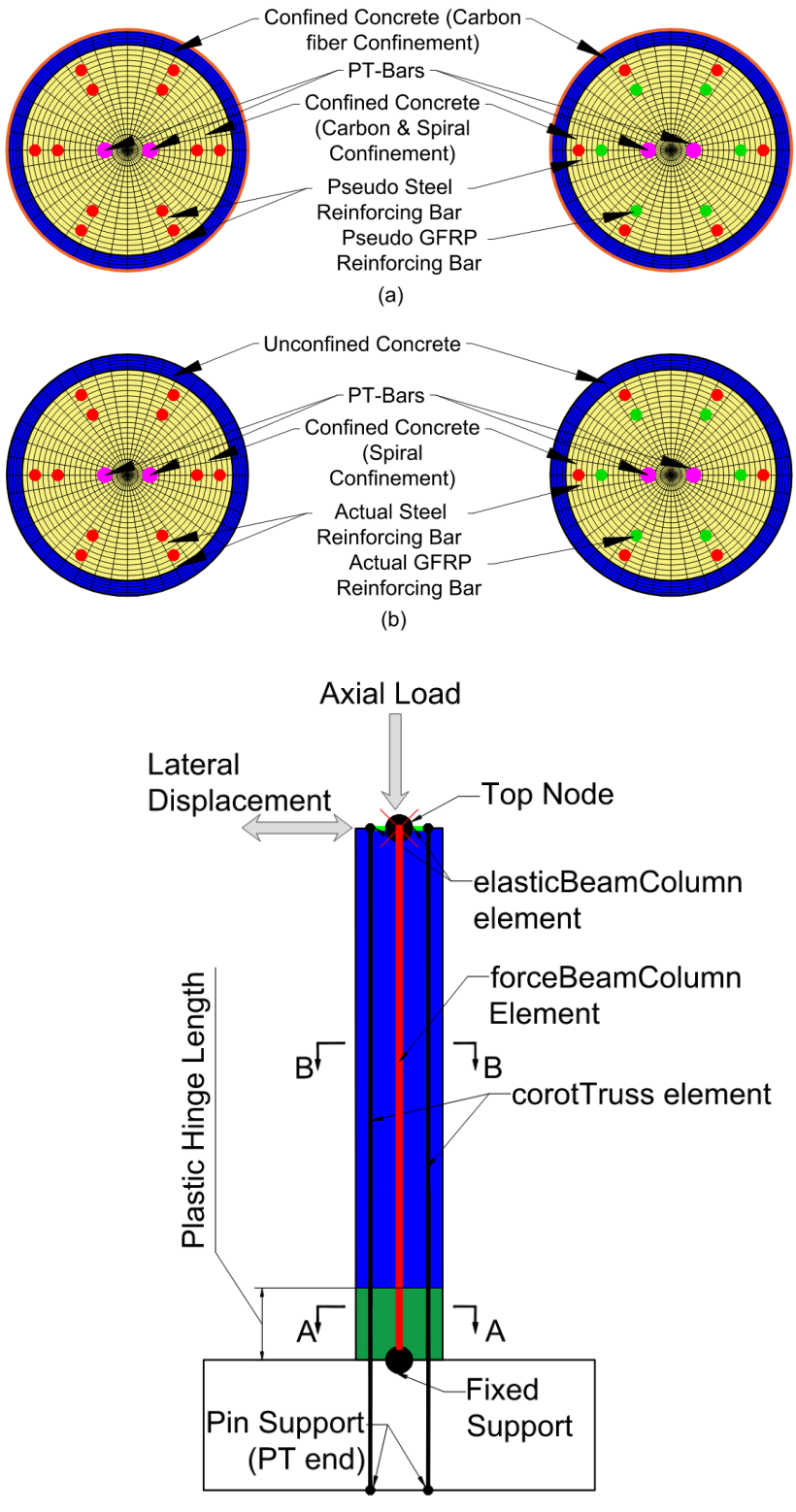

Figure 4.7 Post-tensioned all-steel and hybrid column cross-section and numerical model layout: (a) inside plastic hinge region (section A-A); (b) outside plastic hinge region (section B-B); and (c) model layout

Figure 4.6 shows the numerical model layout for the all-steel (STL) and hybrid column (HYB). Figure 4.7 demonstrates the numerical model layout for the post-tensioned all-steel (PT-STL) and hybrid column (PT-HYB). The column length was segmented into two distinct regions: the first region, located inside the plastic hinge length, utilized the pseudo modulus of elasticity of the reinforcing bars, as illustrated in Figure 4.6(a) and Figure 4.7(a). The second region, located outside the plastic hinge length, used the actual modulus of elasticity of the steel and GFRP reinforcing bars, as shown in Figure 4.6(b) and Figure 4.7(b).

4.5 Plastic Hinge Length (L_p)

The AASHTO Guideline Specifications (2011) and Caltrans Seismic Design Criteria (2013) are used for the design of bridges in the United States. To simulate the experimental performance, the numerical model must be able to estimate the plastic hinge length. An approach by Panagiotakos and Fardis (2001) was used to determine an initial value of the plastic hinge length:

$$L_p = 0.12H + 0.014a_{sl}d_b f_y \quad (7)$$

where, a_{sl} is equal to zero when bar pull-out is restricted and is equal to 1.0 if the reinforcing bar is allowed to pull out; d_b is the longitudinal bar diameter (mm); H is the height of the column specimen (mm); and f_y is the yield strength of the reinforcing bar (MPa). The plastic hinge length of the specimens was calculated using Eq. (7) since sufficient development length was provided and bar pull-out was prevented. The plastic hinge length was computed from Eq. (7) and was found to be 300 mm; the same plastic hinge length was used for all specimens. The calculated length of the plastic hinge was confirmed by calibrating its value so that the hysteresis curve of the numerical model matched the experimental hysteresis while keeping all other parameters constant.

4.6 Analysis

OpenSees was used to carry out the static analysis for both gravity and cyclic loads. The cyclic analysis consisted of applying a monotonically increasing pull to a target drift, reversing the drift to the same magnitude in the reverse direction, and then returning to a zero-drift condition, all in a displacement-controlled manner. Displacement control is implemented by OpenSees through the *DisplacementControl* object for an integrator, which means that every incremental step of the analysis is performed at incremental values of the applied displacements in one degree of freedom. In all the static analyses, the displacement increment was 1.0% of the column height. Convergent methods in finding the solution to nonlinear algebraic equations, namely *Newton*, *Broyden NewtonLineSearch*, and *KrylovNewton*, were used to solve the nonlinear residual solutions at every time increment (Bowman 2016).

4.7 Model Validation

The proposed modeling approach is used to generate hysteresis curves for the four columns subjected to a cyclic load. A comparison is conducted between the hysteresis curves derived from experimental data and numerical simulations. The validation procedure includes evaluating both the overall and local responses of the columns. Key parameters such as initial stiffness, hysteretic energy, and unloading stiffness for the overall response, as well as bar fracture cycle and post-tensioning force level for the local response, are scrutinized to assess how closely the numerical model aligns with the experimental results. To deem the numerical model validation acceptable, the maximum allowable error between the experiment and model is between 10% and 12%, as outlined in Figure 4.8.

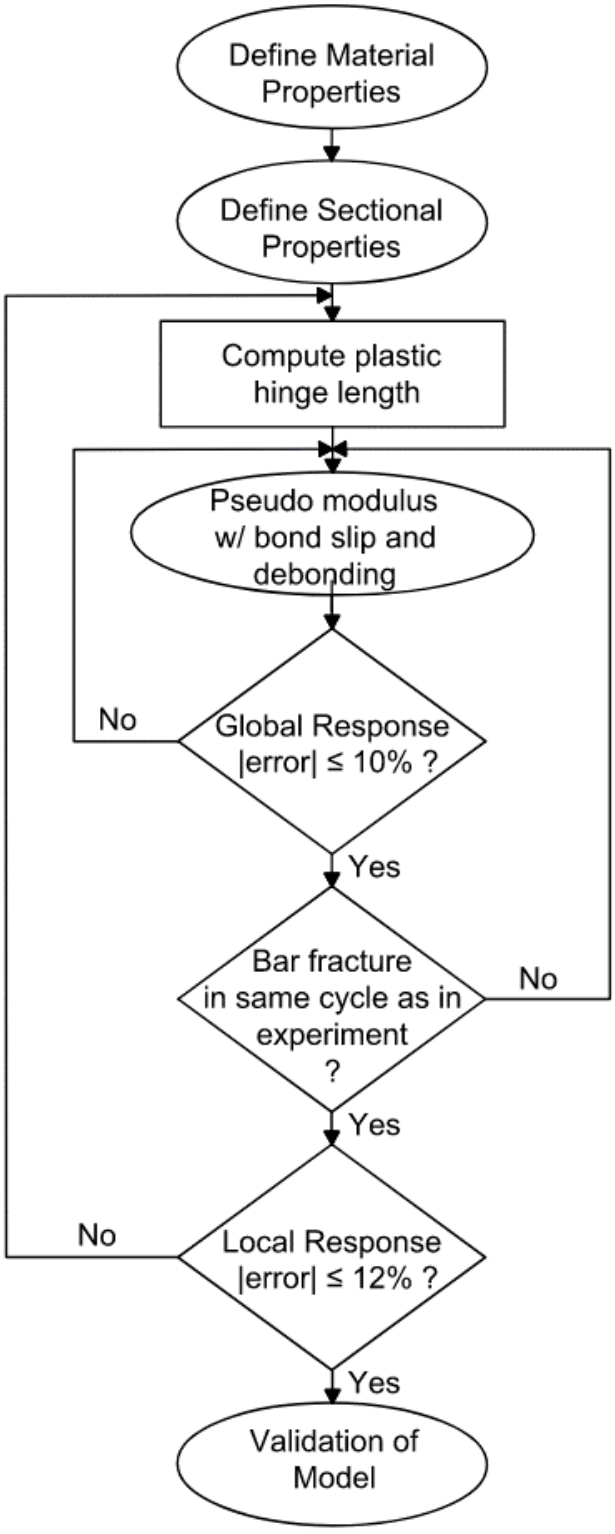

Figure 4.8 Flowchart of numerical model

4.8 Comparison of Experiments and Numerical Model

A comparative analysis was conducted between the model and experiments for global and local response of the four columns. This comparison encompassed parameters such as hysteretic response, cumulative hysteretic energy, and the cycle at which longitudinal bar fracture occurred.

4.8.1 Global Response

Global response includes the hysteretic behavior of the system. The response of the numerical model is assessed in terms of overall hysteresis loops, aiming for agreement with the experiments within an acceptable margin of error. This is achieved by calculating the hysteretic energy, determined as the area inside each hysteresis loop. The overall agreement of the hysteretic curves, including loading and unloading stiffness and hysteretic energy, serves as a benchmark for validating the numerical response in the context of global behavior.

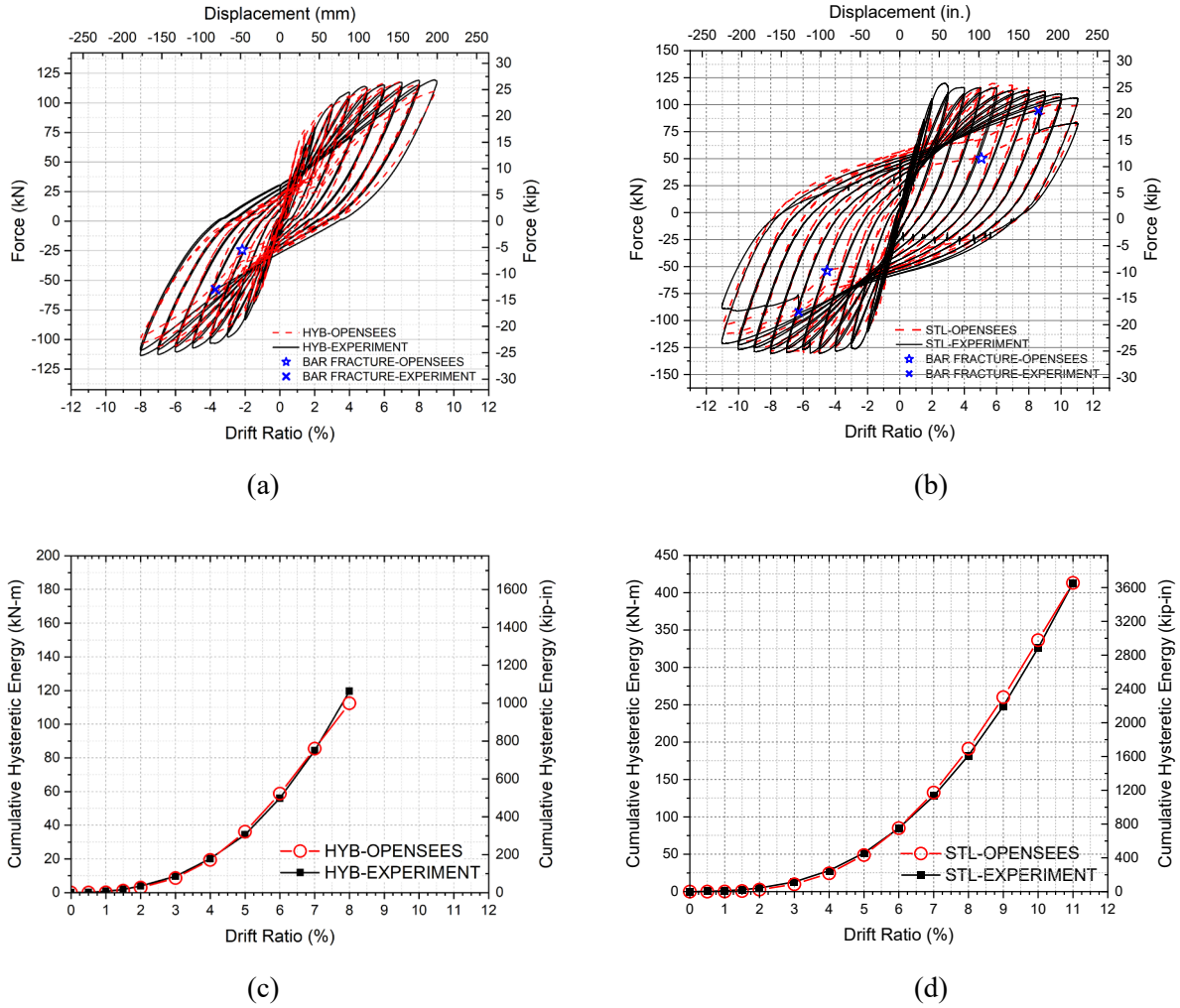

Figure 4.9 All-steel and hybrid column comparison of experiment and OpenSees model: (a) HYB column hysteresis; (b) STL column hysteresis; (c) HYB column hysteretic energy; and (d) STL column hysteretic energy

The numerical model successfully predicted the hysteretic response of columns HYB and STL that were not post-tensioned, as illustrated in Figure 4.9(a, b), with the loading and unloading stiffness of the hysteresis loops showing good agreement with the experiment. The model predicted the maximum lateral load with an error of 3.0% for the HYB column during the 8.0% drift ratio. The model stopped at the first cycle of the 9.0% drift ratio due to GFRP bar fracture in compression. The numerical model captured the initial stiffness of the pull cycles with good accuracy. However, there were some minor differences for the push cycles; one reason for this phenomenon is an initial gap between the loading plate and column top, which caused the column to settle during the first push cycles. For the all-steel STL column, the model predicted the maximum lateral load within 1.0% of the experiment.

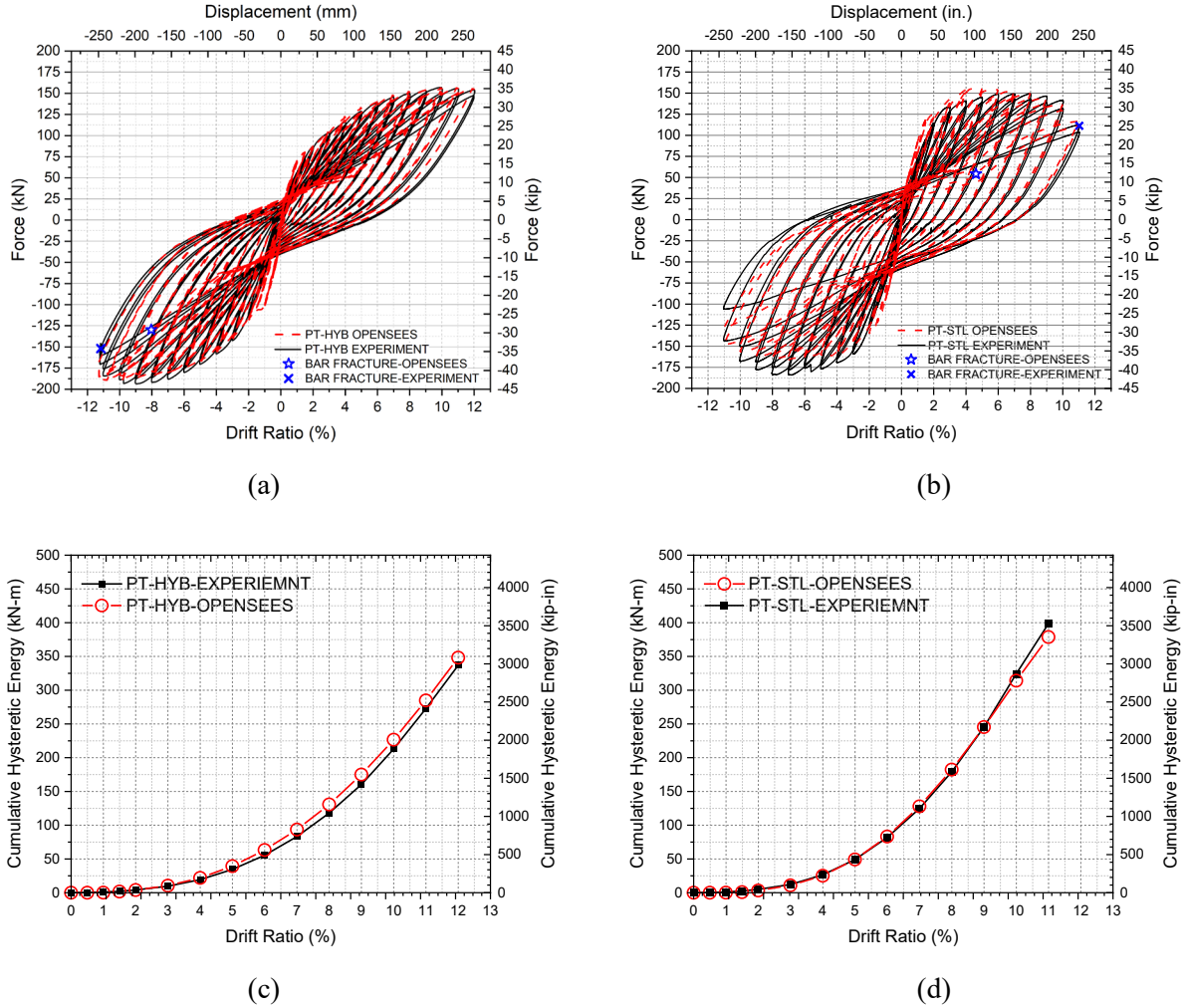

Figure 4.10 Post-tensioned column comparison of experiment and OpenSees model: (a) PT-HYB column hysteresis; (b) PT-STL column hysteresis; (c) PT-HYB column hysteretic energy; and (d) PT-STL column hysteretic energy

The numerical model successfully predicted the hysteretic response of the post-tensioned columns PT-HYB and PT-STL, as shown in Figure 4.10(a, b), with the loading and unloading stiffness of the hysteresis curves showing good agreement with the experimental results. The numerical model successfully captured the initial stiffness, with a 5.0% and 7.5% error for the PT-HYB and PT-STL columns, respectively. The differences are attributed to variations in modeling the supports compared with the actual conditions. The numerical model successfully predicted the maximum drift ratio reached in the experiments before failure based on low cycle fatigue fracture of the steel reinforcing bars.

The hysteretic energy is plotted at each drift ratio for the experiments and the model, as illustrated in Figure 4.9(c, d) for the HYB and STL specimens and Figure 4.10(c, d) for the PT-HYB and PT-STL specimens, respectively. The overall cumulative hysteretic energy in the numerical model displayed an error of 6.0% or less compared with the experiments for all columns. Specifically, the error in hysteretic energy for specimen STL was 0.5%, for HYB it was 6.0%, for PT-STL it was 5.0%, and for PT-HYB it was 3.4% compared with the experiments. These findings indicate good agreement in terms of global response.

4.8.2 Local Response

The local response was assessed based on the drift ratio at which bar fracture occurred. In the experiments, fracture of longitudinal bars occurred during the 9.0% and 11.0% drift ratio for the HYB column and the STL column, respectively. For the post-tensioned column tests, the experiments recorded bar fractures of the PT-HYB and PT-STL columns at 11.0%. The numerical model predicted bar fracture at the same drift ratio as the experiment. Failure in the numerical model occurred at the same cycle as in the experiments, as shown in Figure 4.9(a, b) for columns HYB and STL and in Figure 4.10(a, b) for post-tensioned columns PT-HYB and PT-STL. The model accurately predicted the maximum lateral load with an error of 2.0% for the post-tensioned hybrid (PT-HYB) column and an error of 12.0% for the post-tensioned all-steel (PT-STL) column.

The numerical model predicted the post-tensioning forces for column PT-HYB, as shown in Figure 4.11(a), and column PT-STL, as shown in Figure 4.11(b). The loading and unloading curves are in good agreement with the experimental results. Both columns had a difference of less than 5.0% of the peak post-tensioning force between the numerical model and experimental results. Moreover, none of the PT bars reached yielding, as illustrated in Figure 4.11. For the PT-HYB column, the gap of push cycles of the west PT bars can be justified by the progressive concrete spalling above the CFRP-jacket, resulting in lower PT forces in the experiment than in the model. On the other hand, the east post-tensioning bar in column PT-STL dug into the concrete at the top column and caused a variance in the push cycles.

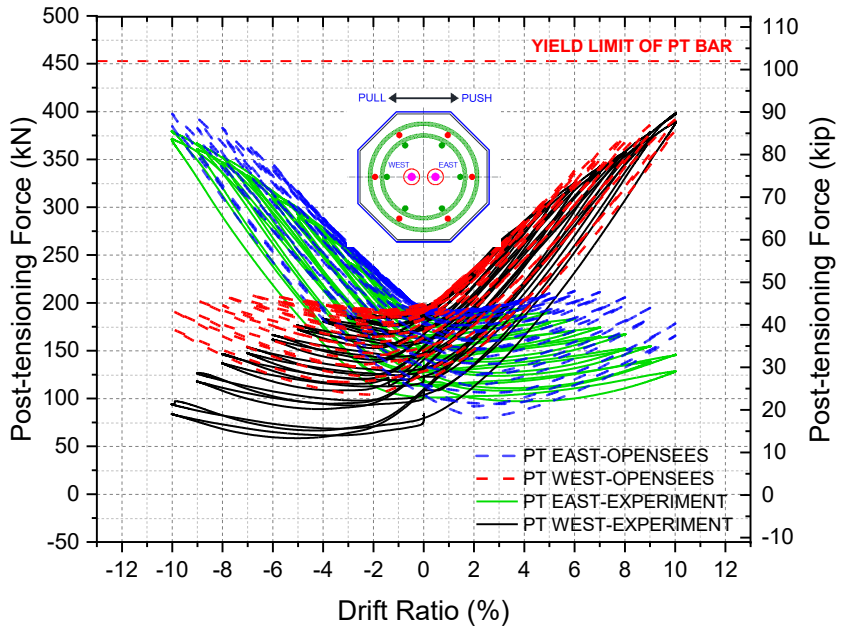

(a)

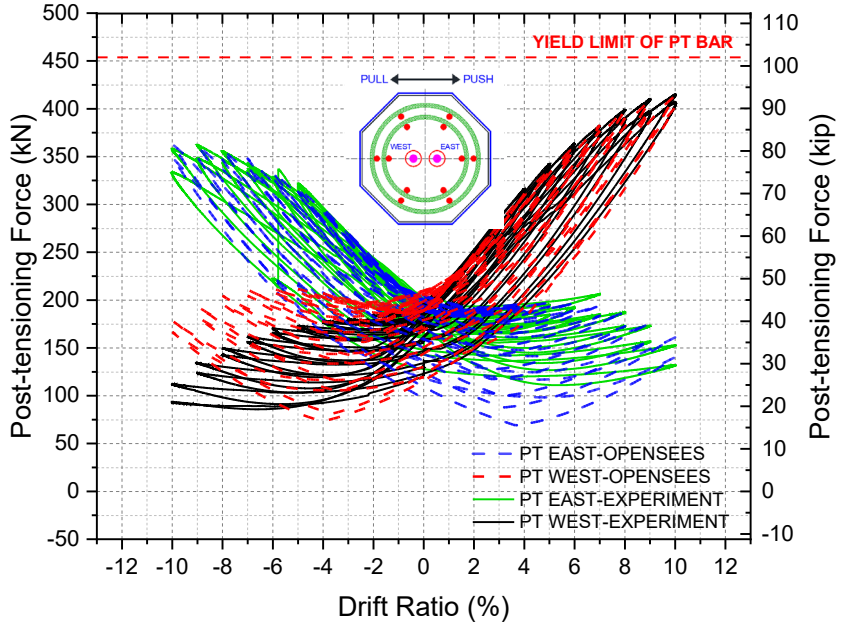

(b)

Figure 4.11 Post-tensioned column comparison of experiment and OpenSees model: (a) PT-HYB column hysteresis; (b) PT-STL column hysteresis; (c) PT-HYB column hysteretic energy; and (d) PT-STL column hysteretic energy

5. PARAMETRIC STUDY

The numerical study conducted on two half-scale specimens accurately predicted the experimental response. To expand the applicability of the numerical model, a parametric study was performed on an as-built two-column bent of the Riverdale Bridge in Ogden, Utah (Thapa and Pantelides 2021). This bridge, constructed using accelerated bridge construction (ABC) techniques with precast concrete columns and cap beams, comprises two main spans, two approach spans, and is supported by three lines of piers, each consisting of four two-column bents, resulting in a total bridge width of 52.07 meters. Each typical bridge bent spans four segments with two columns per segment. The original bridge bent includes a precast concrete cap beam, precast concrete columns, and footings, with 4,877-mm long octagonal columns equipped with six 36 mm diameter, 1,034 MPa threaded PT bars around the perimeter, connecting the cap beam, columns, and footings. These PT bars are grouted inside a 54-mm outside diameter galvanized steel duct in the actual bridge, without additional lateral force-resisting reinforcement since the column mild steel bars do not extend across the column-to-footing or the column-to-cap beam interfaces. The actual geometry of the prototype Riverdale Bridge bent is illustrated in Figure 5.1. The actual dimensions of the Riverdale Bridge bent with grouted duct connection are studied numerically to observe the performance of the bridge bent during cyclic loading. This study includes GFRP spirals with either all-steel longitudinal bar or a hybrid combination of GFRP and mild steel longitudinal bars. Plastic hinge length on the ends of the column was protected using a CFRP jacket to prevent column concrete crushing during lateral load application. Table 5.1 shows material properties and geometrical details used in the parametric study of the actual scale bridge bent.

Table 5.1 Properties used in parametric study

Parameters	**STL**	**HYB**
Stirrup spacing (mm)	152	152
Span (mm)	13945	13945
Column height (mm)	4877	4877
Intentional debonding length (mm)	304	304
Plastic hinge length (mm)	585	585
Modulus of elasticity GFRP (GPa)	41	41
Modified modulus of elasticity GFRP (GPa)	20	20
Modulus of elasticity mild steel (GPa)	200	200
Modified modulus of elasticity mild steel (GPa)	138	138
Concrete compressive strength (f'c) (MPa)	42	42

Two different numerical models were studied for the parametric study:

1. Numerical model with all-steel bars with grouted duct connection and PT bars (STL)

Octagonal columns measuring 4,877 mm in length and featuring six 36-mm diameter threaded PT bars, with a tensile strength of 1,034 MPa, encircling the perimeter, were used alongside twelve 19M mild steel reinforcing bars crossing the interface. These elements, comprising columns, footings, and cap-beams, were used in a parametric study similar to the Riverdale Bridge bent, exploring variations in precast connection systems. Longitudinal reinforcement was confined using 13M GFRP spirals at intervals of 152 mm. These

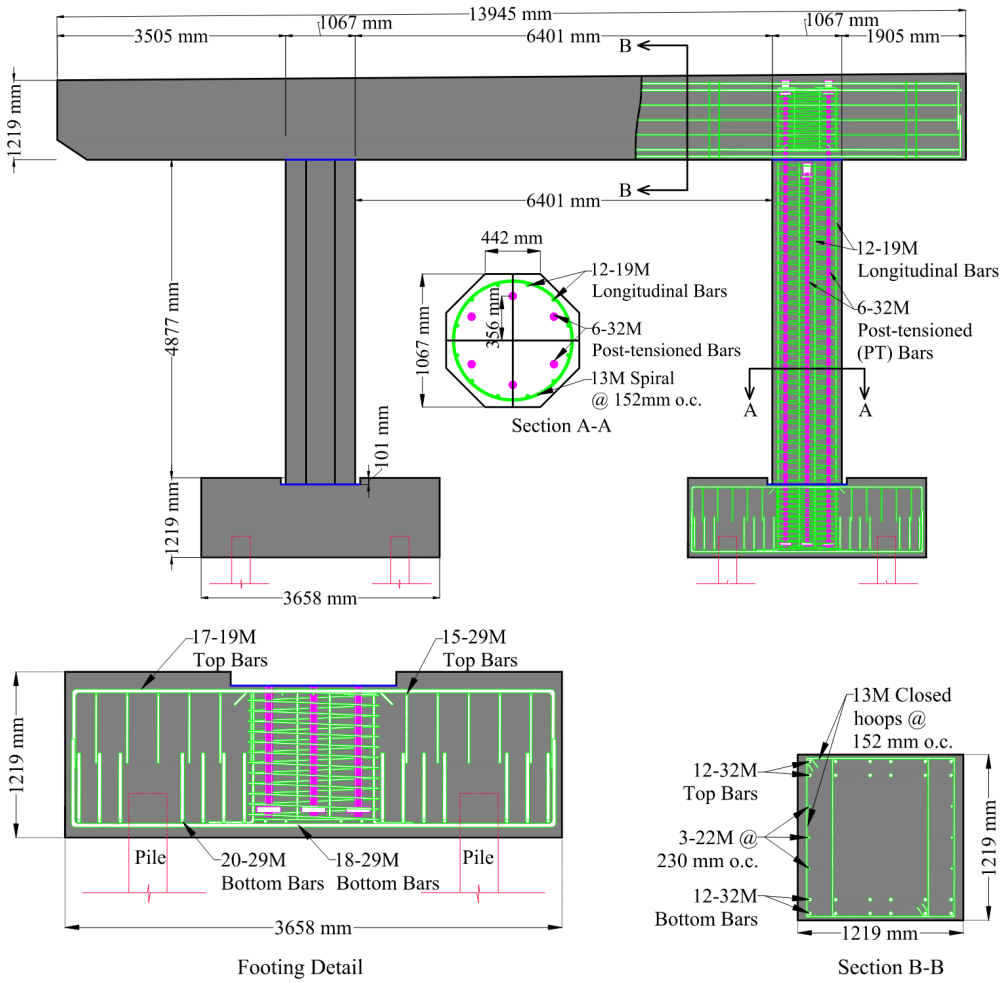

Figure 5.1 Prototype bridge bent of Riverdale Bridge with details

longitudinal bars were connected to the cap beam and footing through grouted duct connections, extending beyond the column ends and housed within galvanized ducts embedded in the footing and cap beam using high-strength grout, as shown in Figure 5.2. The grouted ducts, ensuring a minimum embedment length of eight times the bar diameter, effectively prevented pullout of the longitudinal reinforcing bars. Energy dissipation was facilitated by the grouted longitudinal bars, while the PT bars were assumed to remain unbonded, to assist in self-centering of the bridge bent. Selecting an appropriate initial post-tensioning force was crucial to maintain the PT bars within the elastic range, each bar initially tensioned to 335 kN. Intentional debonding of the longitudinal reinforcing bars occurred within the column and footing, with a debonded length set at eight times the bar diameter ($8d_b$), totaling 304 mm in length, 152 mm of which was in the footing and 152 mm was in the column.

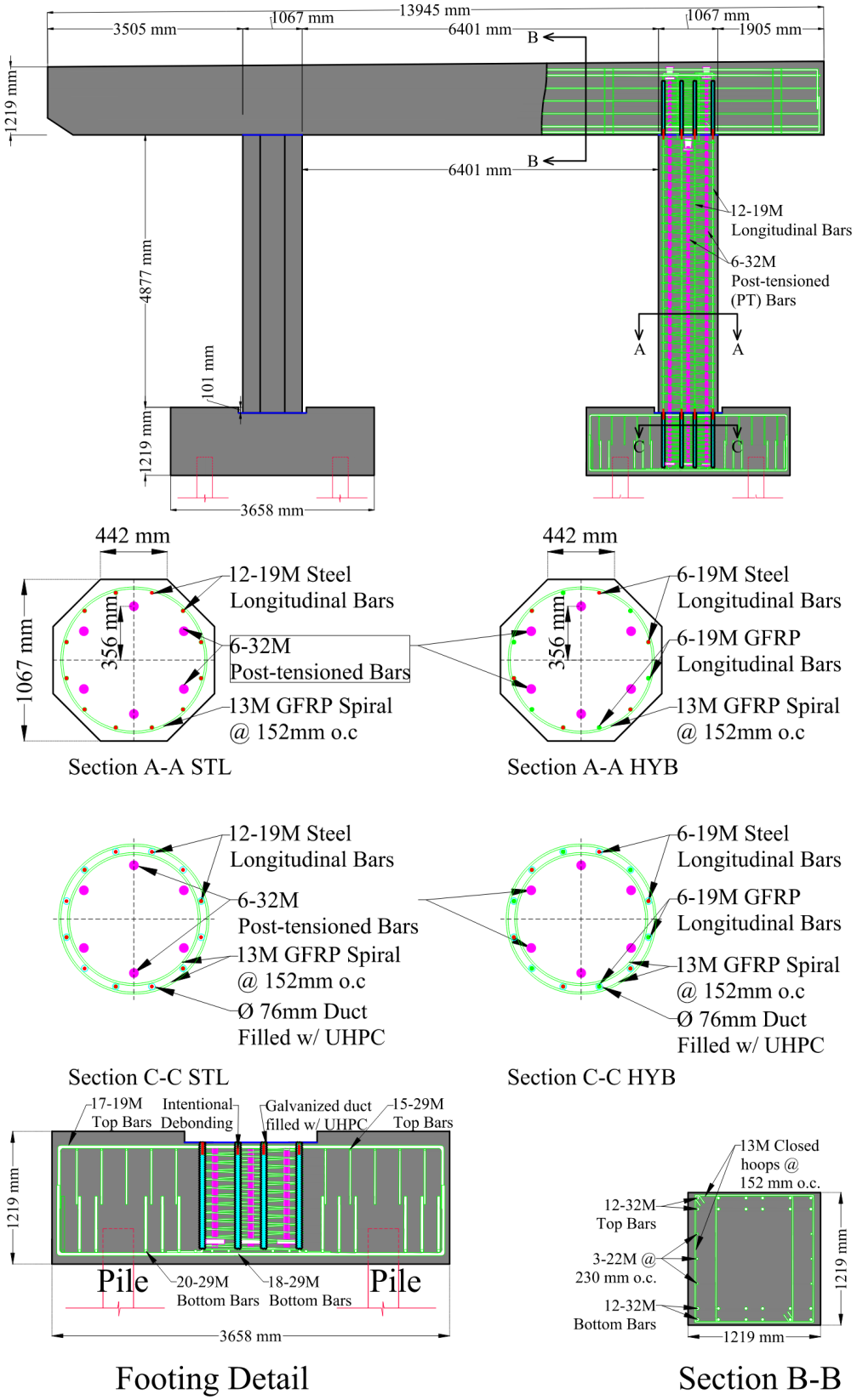

Figure 5.2 Modified Riverdale bridge bent with PT bars and grouted duct connection

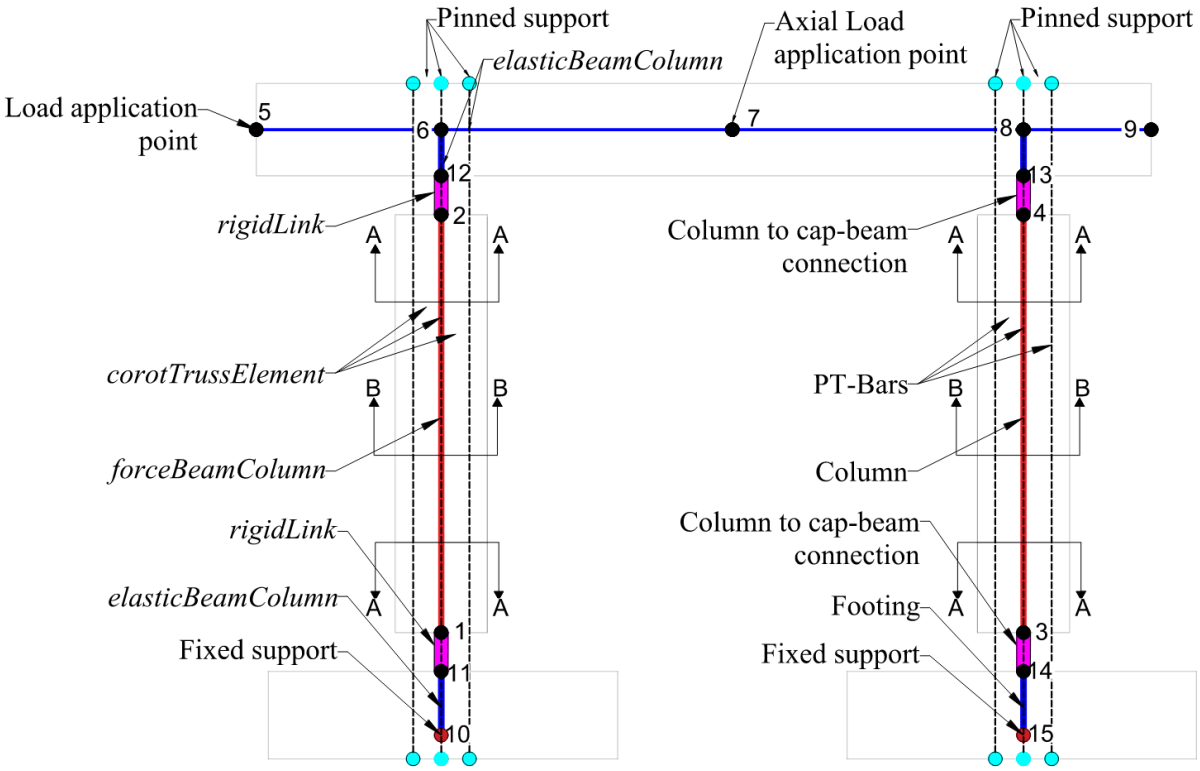

(a)

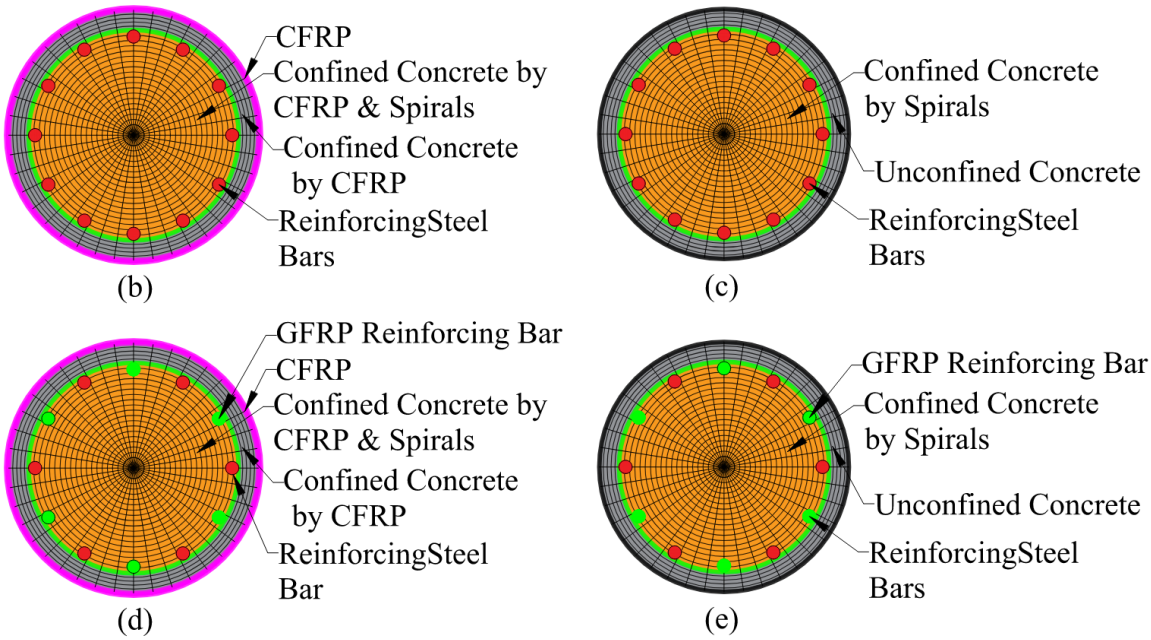

Figure 5.3 Numerical model details: (a) Schematic for numerical model of Riverdale bridge bent; STL column detail: (b) Section A-A; and (c) Section B-B; HYB column detail: (d) Section A-A; and (e) Section B-B

2. **Numerical model with steel bars and GFRP bars with grouted duct connection and PT bars (HYB)**

In a study similar to the Riverdale Bridge bent, octagonal columns measuring 4,877 mm and with six 36-mm diameter threaded PT bars, alongside six 19M mild steel and six 19M GFRP longitudinal reinforcing bars placed alternately to each other, were examined for precast connection variations. Longitudinal reinforcement, confined with 13M GFRP spirals every 152 mm, connected to the cap beam and footing via grouted ducts, extending beyond the column ends. These bars, along with the unbonded PT bars, assisted in self-centering. An initial post-tensioning force of 335 kN was used for each PT bar. Intentionally debonded longitudinal bars within the column and footing, each at eight times the bar diameter ($8d_b$), are used for a total debonded length equal to 304 mm. The construction detail of the bridge bent is shown in Figure 5.2.

5.1 Numerical model

The numerical model used to verify the four previously tested specimens was modified to represent the actual bridge bent. This 2D numerical model included the cap beam and bridge columns. The joints between the columns and the cap beam were defined as rigid joints. Mander's model was applied to characterize the concrete properties using the $Concrete04$ element from OpenSees (Popovics 1973). Steel reinforcing bars were modeled using the $ReinforcingSteel$ material (Kunnath et al. 2009), with different material properties assigned inside and outside the plastic hinge regions. The modified pseudo-reinforcing property due to bond-slip in the actual bridge bent was calculated using the equations in section 4.3. The adjusted modulus of elasticity for the column steel reinforcement in the actual bridge bent was determined to be $138\ GPa$, and this was used to model the reinforcing bars within the plastic hinge regions. The octagonal column section was changed to a circular cross-section of equivalent area for ease of numerical model geometry definition. The circular column cross-section was divided into 15 subdivisions for both the cover and core concrete, both width- and height-wise. The column cap beam and the grade beam connecting the columns to the footing base were modeled as $elasticBeamColumn$ elements (Mazzoni et al. 2006). Rigid links were used to create rigid connections between the column and cap beam. The deck weight, column weight, and cap beam were modeled as nodal mass at each node of the cap beam, with nodal masses of $54\text{x}10^3$ kg for nodes 5 and 9; and $69\text{x}10^3$ kg for nodes 6 and 8. The schematic layout of the numerical model is shown in Figure 5.3. Axial load, crucial for predicting the model's behavior and alignment with experimental results, was applied at 6% of the axial load index (ALI), equivalent to $525\ kN$ per column. Accurately predicting the plastic hinge length (L_p) of the columns is essential. To evaluate the plastic hinge length for the actual as-built bridge bent, the equation proposed by Panagiotakos and Fardis (2001) was used. The plastic hinge length was calculated as 12% of the column length, using Eq. 7 with reinforcing bars restricted against pullout.

Two different numerical models were developed: one model with all steel bars and PT bars and a second model with a hybrid combination and PT bars (Figure 5.3). *Concrete04* was used to model the concrete, accounting for confined cover concrete due to the CFRP wrap and confined core concrete due to both the CFRP jacket and GFRP spirals. Concrete with a compressive strength of 42 MPa was used, and other confinement properties used in the numerical model are illustrated in Figure 5.4(a); Figure 5.4(b) shows the material properties of the PT bars. GFRP bars and steel reinforcing bars featured intentional debonding and bond-slip effects; their modified pseudo modulus of elasticity was calculated as described in earlier sections. These pseudo modulus properties were applied within the plastic hinge region, while the actual properties were used outside this region, as shown in Figure 5.4(c, d).

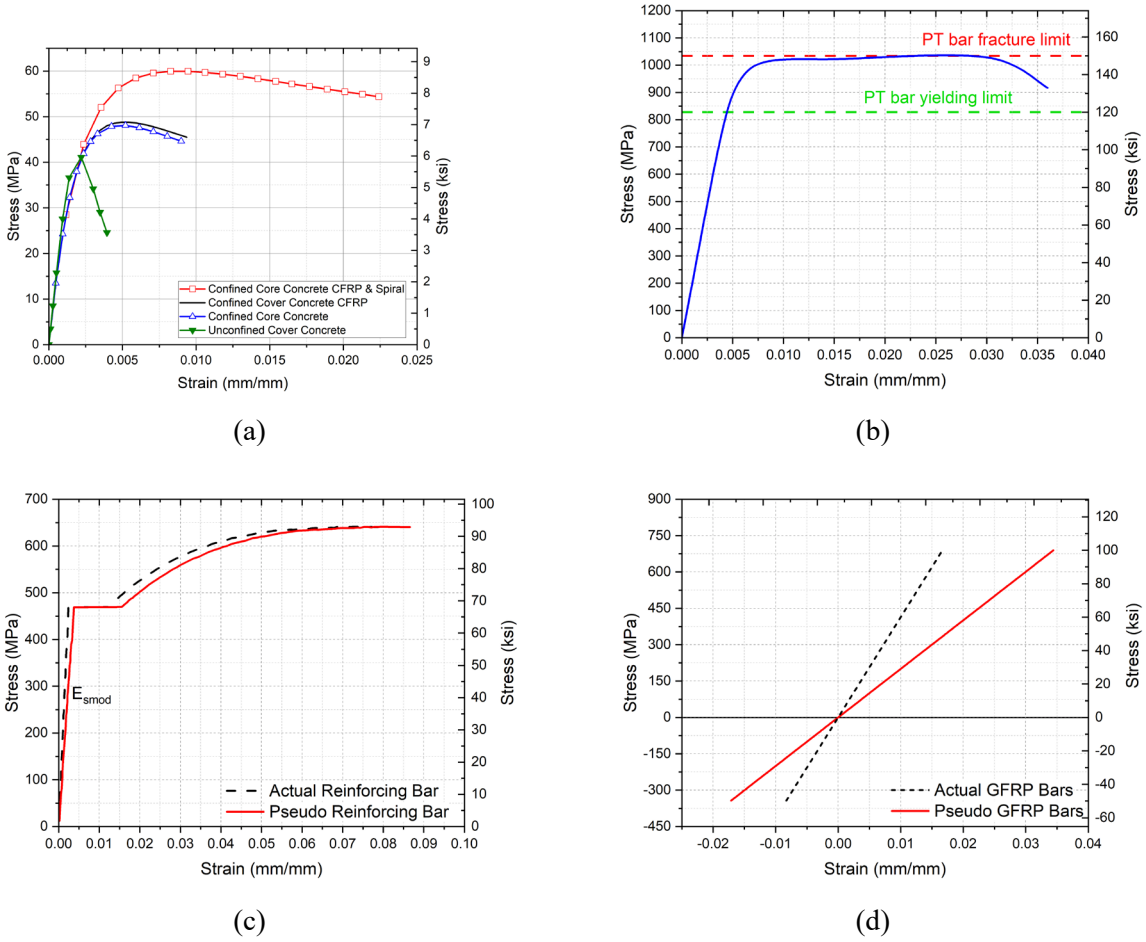

Figure 5.4 Material model details: (a) Concrete; (b) Post tensioning bars; (c) Longitudinal mild-steel reinforcing bars; and (d) GFRP longitudinal reinforcing bar

5.2 Results of Parametric Study

The numerical model, which incorporated the deck weight, underwent cyclic displacement-controlled loading. This approach facilitated the computation of the cyclic response of the bridge bent using previously established techniques. Force versus displacement curves were plotted for both all-steel longitudinal reinforcing bars and hybrid reinforcing bars, revealing their respective hysteretic responses. The analysis revealed that while the lateral load capacities of both bents were nearly identical, their residual displacements differed significantly. The hybrid bent, reinforced with GFRP bars, exhibited superior self-centering capabilities compared with the all-steel reinforced bent.

Cyclic lateral loading was applied until either the post-tensioning (PT) bars yielded, concrete crushing occurred, or reinforcing bar fracture occurred, at which point the model was terminated. The all-steel reinforcing bar model exhibited a residual drift ratio exceeding 1.0% at an applied 3.0% drift ratio, whereas the hybrid setup reached a 1.0% residual displacement only after an applied 4.0% drift ratio. This indicates that the hybrid reinforcing arrangement has superior self-centering performance, supported by experimental studies on scaled specimens as explained in earlier sections. The hysteretic curves for the all-steel bent showed wider loops, suggesting higher hysteretic energy dissipation, while the hybrid combination with steel and GFRP bars had slightly narrower hysteretic loops, indicating lower hysteretic energy dissipation. The choice of reinforcement combination depends on the design requirements. If

higher hysteretic energy dissipation is desired, the all-steel combination can be used, whereas the hybrid combination can be employed for better self-centering performance. Both specimens exhibited similar initial stiffness and peak load. The PT bars started yielding around 1.5% drift ratio for both bents. The longitudinal mild steel reinforcing bars fractured due to low-cycle fatigue at 3.5% drift ratio for the all-steel reinforced bent, whereas the longitudinal mild steel bars fractured at 4.0% drift ratio for the hybrid configuration; and there was no fracture of GFRP bars. Figure 5.5 shows the hysteretic curves for the all-steel and hybrid bridge bents and their hysteretic performance comparison.

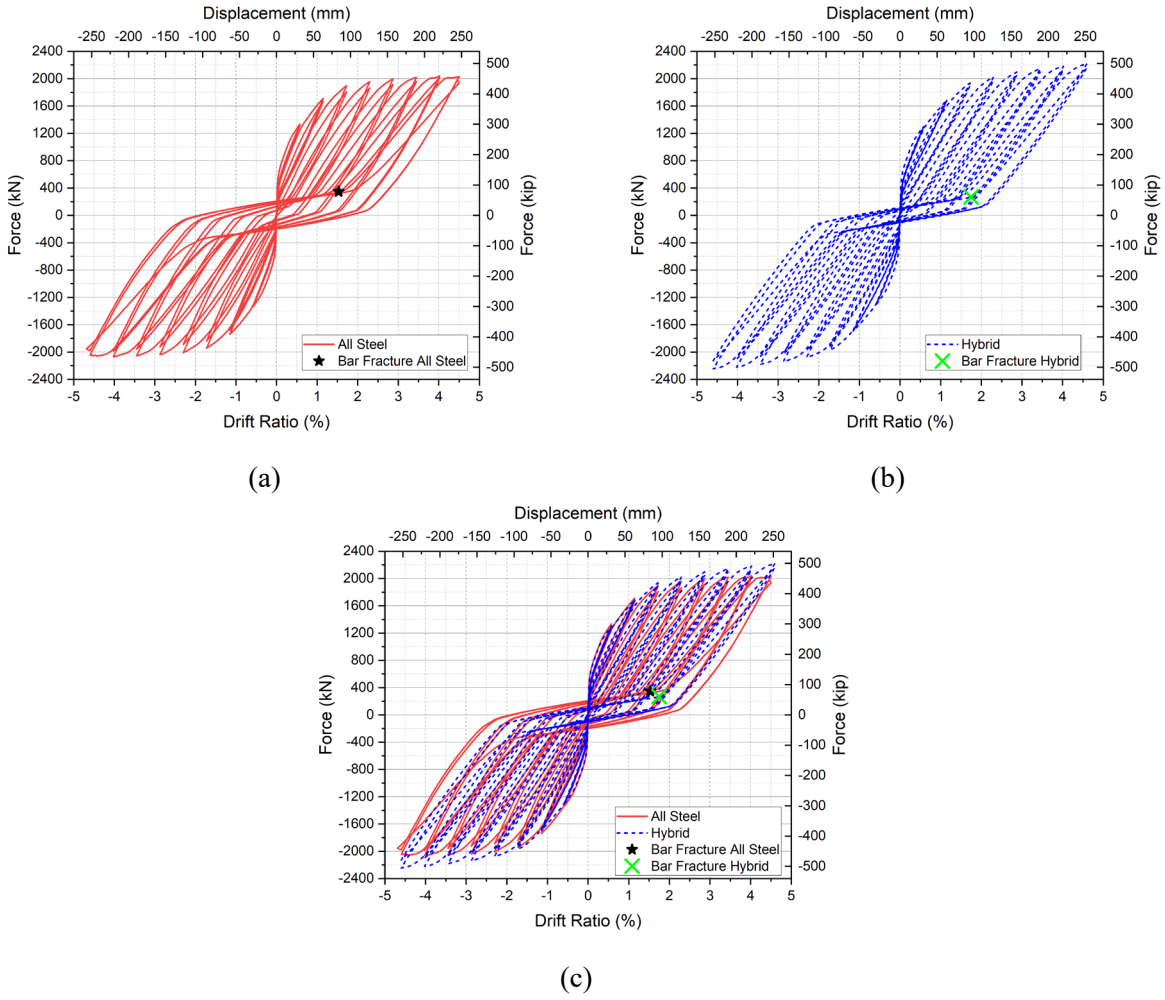

Figure 5.5 Hysteretic response of full scaled bridge bent with post-tensioning bars: (a) Bent with all steel reinforcement configuration; (b) Bent with hybrid reinforcement configuration; and (c) Comparison between all steel and hybrid reinforcement configuration

Once the hysteretic response was obtained, the hysteretic energy was computed as the area under the hysteresis curves, and the cumulative hysteretic energy was calculated at each drift ratio. From the numerical results, it was found that the bridge bent with all-steel reinforcing bars dissipated almost 1.5 times the hysteretic energy of the hybrid specimen, whereas the PT bars yielded around the same time, at an approximately 1.5% drift ratio, for both all-steel and hybrid reinforced bents. The higher energy dissipation by the all-steel bent represents the ability of the longitudinal bars in dissipating hysteretic energy, since the response for the bent with the hybrid reinforcing bar arrangement exhibited a more flag-shaped hysteretic loop compared with the all-steel bent. The flag-shaped hysteretic loop indicates lower energy dissipation but better self-centering capabilities due to the presence of GFRP bars, which have a linear-elastic behavior until failure and do not contribute significantly to energy dissipation through inelastic deformation.

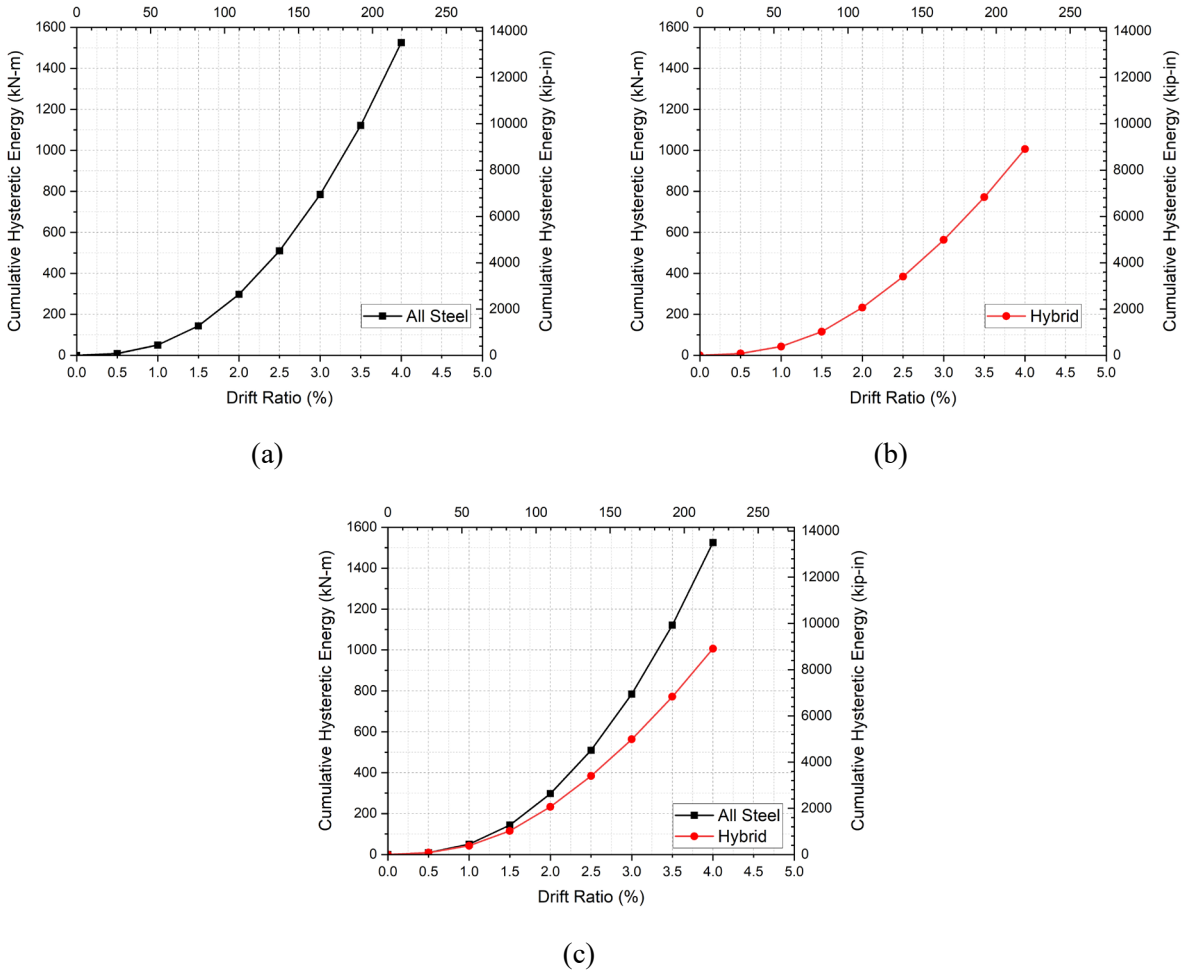

(a) (b)

(c)

Figure 5.6 Hysteretic energy of full scaled bridge bent with post-tensioning bars: (a) Bent with all steel reinforcement configuration; (b) Bent with hybrid reinforcement configuration; and (c) Comparison between all steel and hybrid reinforcement configuration

6. DESIGN RECOMMENDATIONS

Based on the experimental study of half-scaled bridge bents and numerical analysis of an actual bridge bent, the following design recommendations are proposed for precast construction using all-steel and hybrid techniques with and without post-tensioning with grouted duct connections:

- Utilize seismic design guidelines to design individual components of the precast structure, ensuring compliance with relevant codes and standards for seismic performance.
- Precast structures can be connected using either recessed spliced sleeves or grouted duct connections with the required length of embedment. The choice of connection method should be based on constructability, durability, and performance requirements.
- The amount of intentional debonding affects the performance. For better response, it is suggested to carry out intentional debonding inside the footing since this has been shown to improve self-centering capabilities.
- The minimum length of intentional debonding is recommended to be eight times the bar diameter $(8d_b)$ for optimal performance.
- The choice of initial post-tensioning force depends on the self-centering requirement and should be computed based on rigid body analogy so that the PT bars yield after the design drift ratio.
- The use of GFRP reinforcing bars, together with mild steel longitudinal reinforcing bars, reduces residual displacement, exhibiting better self-centering capacity compared with all-steel reinforcement.
- The confinement reinforcement should be continuous from the column to the footing, and high-strength grout must be used to ensure a proper load path and adequate confinement.

By following these design recommendations, precast construction using the proposed techniques can emulate or even improve upon the response of monolithic construction while benefiting from the advantages of precast construction, such as improved quality control, reduced construction time, and enhanced durability.

7. CONCLUSIONS AND RECOMMENDATIONS

7.1 Conclusions

Quasi-static cyclic load tests were conducted on four bridge column-to-footing joint specimens, featuring columns reinforced with either all-steel longitudinal bars (STL) or a combination of steel and GFRP bars (HYB). Additionally, two columns were post-tensioned with high-strength steel bars, with one being all-steel reinforced (PT-STL) and the other hybrid reinforced (PT-HYB). All columns were confined using two layers of GFRP spirals, with the post-tensioned columns receiving extra confinement from an external CFRP jacket. A numerical model was developed to simulate the seismic behavior of these four column-to-footing joint specimens accurately, considering different reinforcement and post-tensioning configurations. The following conclusions were drawn:

1. **Accurate Representation of Cyclic Behavior**: The numerical model, incorporating plastic hinge length, buckling, and low cycle fatigue of intentionally debonded steel reinforcing bars, effectively captured the actual behavior under cyclic loading. It predicted the response of precast columns with grouted ducts in a satisfactory manner. Numerical models for confined concrete, steel/GFRP bars, and post-tensioned bars successfully simulated experimental results.
2. **Influence of Bond-Slip and Debonding**: The model accurately accounted for the effects of bond-slip and intentional debonding of steel and GFRP bars by using modified material properties in the plastic hinge region.
3. **Drift Ratio Predictions**: The model accurately predicted maximum drift ratios before bar fracture: 9.0% for the HYB column, 11.0% for the STL column, and 12.0% for both the PT-HYB and PT-STL columns. These drift ratios exceed the limits recommended in seismic design codes.
4. **Hysteresis Curve Agreement**: The model matched experimental hysteresis curves for both loading and unloading cycles, predicting the maximum lateral load within 3.0% for the HYB column, 1.0% for the STL column, 2.0% for the PT-HYB column, and 12.0% for the PT-STL column. The higher error in the case of PT-STL column is because of the unsymmetrical force distribution seen in the PT bars during the experiment and numerical model.
5. **Bar Fracture Prediction**: Bar fracture predictions were accurate: bar fractures occurred at 9.0% drift ratio for the HYB column and 11.0% drift ratio for the STL column, consistent with experimental results. For post-tensioned columns, first bar fractures were predicted at an 11.0% drift ratio, aligning with experimental observations.
6. **Cumulative Hysteretic Energy**: The numerical model cumulative hysteretic energy deviation was 0.5% for STL, 6.0% for HYB, 5.0% for PT-STL, and 3.4% for PT-HYB, showing a variance of 6.0% or less up to the drift ratio associated with bar fracture, which is accurate.
7. **Post-Tensioning Forces**: The model accurately predicted post-tensioning forces for both the PT-HYB and PT-STL specimens, with less than a 5.0% difference from experimental peak forces. It correctly indicated that none of the PT bars had yielded, matching experimental results.
8. **Plastic Hinge Length**: The plastic hinge length, calibrated to match the hysteretic response, was 300 mm, aligning with predictions from the literature. This value corresponds to the 74% of the column cross-section and the same value was used for all four specimens. This simplified approach to modeling plastic hinges aids in the seismic design and analysis of flexural precast columns with grouted duct connections, whether reinforced with all-steel or hybrid longitudinal bars.

9. **Parametric Study**: Parametric studies of the bridge bent with mild all-steel reinforcing bar and hybrid reinforcing configurations with GFRP and mild steel reinforcing bars along with post-tensioning bars were performed, which showed that the hybrid reinforced bridge bent performs well in self-centering, whereas the all-steel reinforced bridge bent performs well regarding hysteretic energy dissipation.

7.2 Recommendations for Further Research

This research presents a numerical model to predict the behavior of column-to-footing joints in bridge bents with post-tensioning bars, using grouted duct connections and intentional debonding inside the footings. However, the model was validated against only four experiments, which is not optimal. To ensure accuracy in different scenarios, numerous experimental studies are needed for validation, including full-scale experiments. The research only included one parametric study of the bridge bent, which is not sufficient. Additionally, the computational model uses an equivalent circular column, despite the tested columns having an octagonal cross-section, and only one initial post-tensioning stress level was studied. Incorporating automatic discretization of common concrete sections in OpenSees and investigating different initial PT stress levels could potentially improve model accuracy. To further understand precast connections for bridge substructures using grouted duct connections, more experimental studies are required. These should involve testing large-scale subassemblies or connections under various loading conditions, with enhanced grout mix designs, and refinements of the computational model and constitutive laws.

8. REFERENCES

AASHTO. 2011. *AASHTO Guide Specifications for LRFD Seismic Bridge Design*. Washington, DC: AASHTO.

Ameli, M. J., J. E. Parks, D. N. Brown, and C. P. Pantelides. 2015. "Seismic evaluation of grouted splice sleeve connections for reinforced precast concrete column–to–cap beam joints in accelerated bridge construction." *PCI J.*, 60(2): 80–103. https://doi.org/10.15554/pcij.03012015.80.103.

Ameli, M. J., D. N. Brown, J. E. Parks, and C. Pantelides. 2016. "Seismic column-to-footing connections using grouted splice sleeves." *ACI Struct. J.*, 113(5): 1021-1030.https://doi.org/10.14359/51688755.

Ameli, M. J., and C. P. Pantelides. 2017. "Seismic Analysis of Precast Concrete Bridge Columns Connected with Grouted Splice Sleeve Connectors." *J. Struct. Eng.*, 143 (2): 04016176. https://doi.org/10.1061/(asce)st.1943-541x.0001678.

Barton, R. D., M. J. Ameli, and C. P. Pantelides. 2022. "Precast concrete bridge column-footing connections with recessed grouted splice sleeve connectors." *ACI Struct. J.*, 119(1): 215-226. http://dx.doi.org/10.14359/51734218.

Brenes, F. J., Wood, S. L., and Kreger, M. E. 2006. "Anchorage Requirements for Grouted Vertical-Duct Connectors in Precast Bent Cap Systems." *Report No. FHWA/TX-06/0-4176-1*, Center for Transportation Research, University of Texas at Austin.

Bowman, B. W. (2016). "Modeling of Post-Tensioned Rocking Bridge Columns." MS Thesis, University of Colorado, Boulder, CO.

California Department of Transportation. 2013. Seismic design criteria. Version 1.7. California Department of Transportation. Sacramento, CA.

Dangol, I., and C.P. Pantelides. 2022. "Resilient posttensioned bridge bent with buckling restrained brace." *J. Bridge Eng.*, 27(2): 04021107. https://doi.org/10.1061/(ASCE)BE.1943-5592.0001823.

Dangol, I., and C. P. Pantelides. 2023. "Seismic analysis of posttensioned and hybrid bridge bents with buckling restrained braces." *J. Bridg. Eng.*, 28(2): 1–15. https://doi.org/10.1061/jbenf2.beeng-5764.

Dhakal, R. P., and K. Maekawa. 2002. "Modeling for Postyield Buckling of Reinforcement." *J. Struct. Eng.*, 128(9): 1139–1147. https://doi.org/10.1061/(asce)0733-9445(2002)128:9(1139).

Elsayed, W. M., M. A. N. Abdel Moaty, and M. E. Issa. 2016. "Effect of reinforcing steel debonding on RC frame performance in resisting progressive collapse." *HBRC J.*, 12 (3): 242–254. Housing and Building National Research Center. https://doi.org/10.1016/j.hbrcj.2015.02.005.

Erkmen, B., and A. E. Schultz. 2009. "Self-centering behavior of unbonded, post-tensioned precast concrete shear walls. *J. of Earthq. Eng.*, 13: 1047-1064. https://doi.org/10.1080/13632460902859136.

Guerrini, G., Restrepo, J. I., Massari, M., and Vervelidis, A. (2014). "Seismic Behavior of Posttensioned Self-Centering Precast Concrete Dual-Shell Steel Columns." *Journal of Structural Engineering*, 141(4), 04014115.

Haber, Z. B., M. S. Saiidi, and D. H. Sanders. 2013. "Precast column footing connections for accelerated bridge construction in seismic zones." Rep. No. CCEER 13-08, Center for Civil Eng. Earthq. Research, Dept. of Civil and Env. Eng., Univ. of Nevada, Reno, NV.

Haber, Z. B., M. S. Saiidi, and D. H. Sanders. 2014. "Seismic performance of precast columns with mechanically spliced column-footing connections." *ACI Struct. J.*, 111(3): 639–650. https://doi.org/10.14359/51686624.

Haber, Z. B., M. Saiid Saiidi, and D. H. Sanders. 2015. "Behavior and simplified modeling of mechanical reinforcing bar splices." *ACI Struct. J.*, 112(2): 179–188. https://doi.org/10.14359/51687455.

Khaleghi, B., E. Schultz, S. Seguirant, L. Marsh, O. Haraldsson, M. Eberhard, and J. Stanton. 2012. "Accelerated bridge construction in Washington state: From research to practice." *PCI J.*, 57 (4): 34–49. https://doi.org/10.15554/pcij.09012012.34.49.

Kunnath, S. K., Y. Heo, and J. F. Mohle. 2009. "Nonlinear uniaxial material model for reinforcing steel bars." *J. Struct. Eng.*, 135 (4): 335–343. https://doi.org/10.1061/(asce)0733-9445(2009)135:4(335).

Kurama, Y. C., S. Sritharan, R. B. Fleischman, J. I. Restrepo, R. S. Henry, N. M. Cleland, S. K. Ghosh, and P. Bonelli. 2018. "Seismic-resistant precast concrete structures: state of the art." *J. Struct. Eng.*, 144(4): 03118001. https://doi.org/10.1061/(asce)st.1943-541x.0001972.

Lee, W. K., and Billington, S. L. 2009. "Simulation and Performance-Based Earthquake Engineering Assessment of Self-Centering Post-Tensioned Concrete Bridge Systems." *PEER Report 2009/109*, Pacific Earthquake Engineering Research Center, University of California, Berkeley, CA.

Lee, D., and D. P. Taylor. 2001. "Viscous damper development and future trends." *Struct. Des. Tall Build.*, 10 (5): 311–320. https://doi.org/10.1002/tal.188.

Mander, J. B., and Cheng, C. T. 1997. "Seismic Resistance of Bridge Piers Based on Damage Avoidance Design." *Technical Report NCEER-97-0014*, National Center for Earthquake Engineering Research,University at Buffalo, NY.

Mander, J. B., M. J. N. Priestley, and R. Park. 1988. "Theoretical Stress-Strain Model For Confined Concrete." *J. Struct. Eng.*, 114 (8): 1804–1826.

Manson, S. S. 1965. "Fatigue: a complex subject—Some simple approximations." *Exp. Mech.*, 5(4), 193–226. https://doi.org/10.1007/BF02321056

Matsumoto, E. 2009. "Emulative precast bent cap connections for seismic regions: grouted duct and cap pocket test results, design and construction specifications, design examples and connection details." Report No. ECS-CSUS-2009-05. California State University, Sacramento.

Mazzoni, S., F. McKenna, M. H. Scott, and G. L. Fenves. 2006. "Open System for Earthquake Engineering Simulation (OpenSEES) user command-language manual." *Pacific Earthq. Eng. Res. Cent.*, Univ. of California, Berkeley, CA.

McKenna, F., M. H. Scott, and G. L. Fenves. 2010. "Nonlinear finite-element analysis software architecture using object composition." *J. Comput. Civ. Eng.*, 24 (1): 95–107. https://doi.org/10.1061/(asce)cp.1943-5487.0000002.

Moran, D.A., C. P. Pantelides, and L. D. Reaveley. 2019. "Mohr-Coulomb model for rectangular and square FRP-confined concrete." *Composite Structures*, 209, 889-904. https://doi.org/10.1016/j.compstruct.2018.11.024

Motaref, S., Saiidi, M. S., and Sanders, D. H. (2011). "Seismic Response of Precast Columns with Energy Dissipating Joints." *Report No. CA12-1999*, Center for Civil Engineering Earthquake Research, Department of Civil Engineering, University of Nevada, Reno, NV.

Neupane, S., M. J. Ameli, and C. P. Pantelides. 2023. "Numerical modeling of column piers with recessed spliced sleeves and intentional debonding for accelerated bridge construction." *J. Struct. Eng.*, 149 (3): 1–18. https://doi.org/10.1061/jsendh.steng-11769.

Neupane, S., and C. P. Pantelides. 2024a. "Experiments and Numerical Analysis of a Seismically Resilient Bridge Bent with Stretch Length Anchors as Energy Dissipators." *J. Bridg. Eng.* https://doi.org/10.1061/JBENF2/BEENG-6453.

Neupane, S., and C. P. Pantelides. 2024b. "Hybrid bridge bent using stretch length anchors with post-tensioning and shear key alternatives." *Eng. Struct.*, 310 (April): 118144. Elsevier Ltd. https://doi.org/10.1016/j.engstruct.2024.118144.

Panagiotakos, T. B., and M. N. Fardis. 2001. "Deformations of reinforced concrete members at yielding and ultimate." *ACI Struct. J.*, 98(2): 135–148. https://doi.org/10.14359/10181.

Pang, J. B. K., M. O. Eberhard, and J. F. Stanton. 2010. "Large-bar connection for precast bridge bents in seismic regions." *J. Bridg. Eng.*, 15 (3): 231–239. https://doi.org/10.1061/(asce)be.1943 5592.0000081.

Pantelides C.P., M. E. Gibbons, and L. D. Reaveley. 2013. "Axial load behavior of concrete columns confined with GFRP spirals." *J. Compos. for Constr.*; 17(3):305–313. https://doi.org/10.1061/(ASCE)CC.1943-5614.0000357.

Popovics, S. 1973. "A numerical approach to the complete stress-strain curve of concrete." *Cem. Concr. Res.*, 3 (5): 583–599. https://doi.org/https://doi.org/10.1016/0008-8846(73)90096-3.

Priestley, M. J. N., F. Seible, and G. M. Calvi. 1996. *Seismic Design and Retrofit of Bridges*. John Wiley And Sons. https://doi.org/10.1002/9780470172858.

Raynor, D. J., Lehman, D. E., and Stanton, J. F. 2002. "Bond-slip response of reinforcing bars grouted in ducts." *ACI Structural Journal*, 99(5), 568–576.
Restrepo, J., Matsumoto, E., and Tobolski, M. 2011. "NCHRP Report 681: Development of precast bent cap systems for seismic regions." Transportation Research Board, National Academies, Washington, DC.
Sankholkar, P., C. P. Pantelides, and T. Hales. 2018. "Confinement model for concrete columns reinforced with GFRP spirals." *J. Compos for Constr.* 22(3): 04018007. https://doi.org/10.1061/(ASCE)CC.1943-5614.0000843.
Scott, M. H. 2011. "Numerical integration options for force-based beam-column element in OpenSees." Oregon State Univ., Corvallis, OR.
Shrestha, S., and C. P. Pantelides. 2024. "Cyclic Tests and Analysis of Corroded Precast Concrete Column-to-Footing Connections Constructed with Accelerated Bridge Construction Methods." *J. Bridg. Eng.*, 29 (6): 4024028. American Society of Civil Engineers. https://doi.org/10.1061/JBENF2.BEENG-6632.
Steuck, K. P., Eberhard, M. O., and Stanton, J. F. 2009. "Anchorage of large-diameter reinforcing bars in ducts." *ACI Structural Journal*, 106(4), 506–513.
Tazarv, M., and M. S. Saiidi. 2015. "UHPC-filled duct connections for accelerated bridge construction of RC columns in high seismic zones." *Eng. Struct.*, 99: 413–422. https://doi.org/10.1016/j.engstruct.2015.05.018.
Tazarv, M., and M. S. Saiidi. 2016. "Low-damage precast columns for accelerated bridge construction in high seismic zones." *J. Bridg. Eng.*, 21 (3): 04015056. https://doi.org/10.1061/(ASCE)be.1943-5592.0000806.
Thapa, D., and C. P. Pantelides. 2021. "Self-Centering Bridge Bent with Stretch Length Anchors as a Tension-Only Hysteretic Hybrid System." *J. Struct. Eng.*, 147 (10): 04021163. https://doi.org/10.1061/(asce)st.1943-541x.0003146.
Tran, D., and C. P. Pantelides. 2024a. "Seismic Column-To-Footing Connections Reinforced with Steel/GFRP Bars and GFRP Spirals." *Eng. Struct.*, 305:117788. https://doi.org/10.1016/j.engstruct.2024.117788
Tran, D. Q., and C. P. Pantelides. 2024b. "Seismic Performance of Self-Centering Post-Tensioned Concrete Columns Reinforced with Steel–GFRP Bars and GFRP Spirals." *J. Bridg. Eng.*, 29 (8): 4024055. American Society of Civil Engineers. https://doi.org/10.1061/JBENF2.BEENG-6715.
Wang, Z., Li, T., Qu, H., Wei, H., and Li, Y. (2019). "Seismic Performance of Precast Bridge Columns with Socket and Pocket Connections Based on Quasi-Static Cyclic Tests: Experimental and Numerical Study." *Journal of Bridge Engineering*, 24(11), 04019105.
Wright, J. W., and C. P. Pantelides. 2021. "Axial compression capacity of concrete columns reinforced with corrosion-resistant hybrid reinforcement." *Constr. and Build. Mater.*, 302: 124209. https://doi.org/10.1016/j.conbuildmat.2021.124209.
Zhuo, W., T. Tong, and Z. Liu. 2019. "Analytical pushover method and hysteretic modeling of precast segmental bridge piers with high-strength bars based on cyclic loading test." *J. Struct. Eng.*, 145(7): 04019050. https://doi.org/10.1061/(ASCE)ST.1943-541X.0002318.